DESY 98-085

DESY 98-085

# Measurement of inclusive $D^{*\pm}$ and associated dijet cross sections in photoproduction at HERA

ZEUS Collaboration



**Abstract**

Inclusive photoproduction of $D^{*\pm}$ mesons has been measured for photon-proton centre-of-mass energies in the range $130 < W < 280\,\mathrm{GeV}$ and photon virtuality $Q^2 < 1\,\mathrm{GeV}^2$. The data sample used corresponds to an integrated luminosity of 37 $\mathrm{pb}^{-1}$. Total and differential cross sections as functions of the $D^*$ transverse momentum and pseudorapidity are presented in restricted kinematical regions and the data are compared with next-to-leading order (NLO) perturbative QCD calculations using the "massive charm" and "massless charm" schemes. The measured cross sections are generally above the NLO calculations, in particular in the forward (proton) direction. The large data sample also allows the study of dijet production associated with charm. A significant resolved as well as a direct photon component contribute to the cross section. Leading order QCD Monte Carlo calculations indicate that the resolved contribution arises from a significant charm component in the photon. A massive charm NLO parton level calculation yields lower cross sections compared to the measured results in a kinematic region where the resolved photon contribution is significant.

# The ZEUS Collaboration

J. Breitweg, M. Derrick, D. Krakauer, S. Magill, D. Mikunas, B. Musgrave, J. Repond, R. Stanek, R.L. Talaga, R. Yoshida, H. Zhang
*Argonne National Laboratory, Argonne, IL, USA* [p]

M.C.K. Mattingly
*Andrews University, Berrien Springs, MI, USA*

F. Anselmo, P. Antonioli, G. Bari, M. Basile, L. Bellagamba, D. Boscherini, A. Bruni, G. Bruni, G. Cara Romeo, G. Castellini[1], L. Cifarelli[2], F. Cindolo, A. Contin, N. Coppola, M. Corradi, S. De Pasquale, P. Giusti, G. Iacobucci, G. Laurenti, G. Levi, A. Margotti, T. Massam, R. Nania, F. Palmonari, A. Pesci, A. Polini, G. Sartorelli, Y. Zamora Garcia[3], A. Zichichi
*University and INFN Bologna, Bologna, Italy* [f]

C. Amelung, A. Bornheim, I. Brock, K. Cobö ken, J. Crittenden, R. Deffner, M. Eckert, M. Grothe[4], H. Hartmann, K. Heinloth, L. Heinz, E. Hilger, H.-P. Jakob, A. Kappes, U.F. Katz, R. Kerger, E. Paul, M. Pfeiffer, H. Schnurbusch, H. Wieber
*Physikalisches Institut der Universität Bonn, Bonn, Germany* [c]

D.S. Bailey, S. Campbell-Robson, W.N. Cottingham, B. Foster, R. Hall-Wilton, G.P. Heath, H.F. Heath, J.D. McFall, D. Piccioni, D.G. Roff, R.J. Tapper
*H.H. Wills Physics Laboratory, University of Bristol, Bristol, U.K.* [o]

M. Capua, L. Iannotti, A. Mastroberardino, M. Schioppa, G. Susinno
*Calabria University, Physics Dept.and INFN, Cosenza, Italy* [f]

J.Y. Kim, J.H. Lee, I.T. Lim, M.Y. Pac[5]
*Chonnam National University, Kwangju, Korea* [h]

A. Caldwell[6], N. Cartiglia, Z. Jing, W. Liu, B. Mellado, J.A. Parsons, S. Ritz[7], S. Sampson, F. Sciulli, P.B. Straub, Q. Zhu
*Columbia University, Nevis Labs., Irvington on Hudson, N.Y., USA* [q]

P. Borzemski, J. Chwastowski, A. Eskreys, J. Figiel, K. Klimek, M.B. Przybycień, L. Zawiejski
*Inst. of Nuclear Physics, Cracow, Poland* [j]

L. Adamczyk[8], B. Bednarek, M. Bukowy, A.M. Czermak, K. Jeleń, D. Kisielewska, T. Kowalski,
M. Przybycień, E. Rulikowska-Zarębska, L. Suszycki, J. Zając
*Faculty of Physics and Nuclear Techniques, Academy of Mining and Metallurgy, Cracow, Poland* [j]

Z. Duliński, A. Kotański
*Jagellonian Univ., Dept. of Physics, Cracow, Poland* [k]

G. Abbiendi[9], L.A.T. Bauerdick, U. Behrens, H. Beier[10], J.K. Bienlein, K. Desler, G. Drews, U. Fricke, I. Gialas[11], F. Goebel, P. Göttlicher, R. Graciani, T. Haas, W. Hain, G.F. Hartner, D. Hasell[12], K. Hebbel, K.F. Johnson[13], M. Kasemann, W. Koch, U. Kötz, H. Kowalski, L. Lindemann, B. Löhr, M. Martínez, J. Milewski, M. Milite, T. Monteiro[14], D. Notz, A. Pellegrino, F. Pelucchi, K. Piotrzkowski, M. Rohde, J. Roldán[15], J.J. Ryan[16], P.R.B. Saull, A.A. Savin, U. Schneekloth, O. Schwarzer, F. Selonke, S. Stonjek, B. Surrow[17], E. Tassi, D. Westphal[18], G. Wolf, U. Wollmer, C. Youngman, W. Zeuner
*Deutsches Elektronen-Synchrotron DESY, Hamburg, Germany*

B.D. Burow, C. Coldewey, H.J. Grabosch, A. Meyer, S. Schlenstedt
*DESY-IfH Zeuthen, Zeuthen, Germany*

G. Barbagli, E. Gallo, P. Pelfer
*University and INFN, Florence, Italy* [f]

G. Maccarrone, L. Votano
*INFN, Laboratori Nazionali di Frascati, Frascati, Italy* [f]

A. Bamberger, S. Eisenhardt, P. Markun, H. Raach, T. Trefzger[19], S. Wölfle
*Fakultät für Physik der Universität Freiburg i.Br., Freiburg i.Br., Germany* [c]

J.T. Bromley, N.H. Brook, P.J. Bussey, A.T. Doyle[20], S.W. Lee, N. Macdonald, G.J. McCance, D.H. Saxon,
L.E. Sinclair, I.O. Skillicorn, E. Strickland, R. Waugh
*Dept. of Physics and Astronomy, University of Glasgow, Glasgow, U.K.* [o]

I. Bohnet, N. Gendner, U. Holm, A. Meyer-Larsen, H. Salehi, K. Wick
*Hamburg University, I. Institute of Exp. Physics, Hamburg, Germany* [c]

A. Garfagnini, L.K. Gladilin[21], D. Kçira[22], R. Klanner, E. Lohrmann, G. Poelz, F. Zetsche
*Hamburg University, II. Institute of Exp. Physics, Hamburg, Germany* [c]

T.C. Bacon, I. Butterworth, J.E. Cole, G. Howell, L. Lamberti[23], K.R. Long, D.B. Miller, N. Pavel, A. Prinias[24], J.K. Sedgbeer, D. Sideris, R. Walker
*Imperial College London, High Energy Nuclear Physics Group, London, U.K.* [o]

U. Mallik, S.M. Wang, J.T. Wu[25]
*University of Iowa, Physics and Astronomy Dept., Iowa City, USA* [p]

P. Cloth, D. Filges
*Forschungszentrum Jülich, Institut für Kernphysik, Jülich, Germany*

J.I. Fleck[17], T. Ishii, M. Kuze, I. Suzuki[26], K. Tokushuku, S. Yamada, K. Yamauchi, Y. Yamazaki[27]
*Institute of Particle and Nuclear Studies, KEK, Tsukuba, Japan* [g]

S.J. Hong, S.B. Lee, S.W. Nam[28], S.K. Park
*Korea University, Seoul, Korea* [h]

H. Lim, I.H. Park, D. Son
*Kyungpook National University, Taegu, Korea* [h]

F. Barreiro, J.P. Fernández, G. García, C. Glasman[29], J.M. Hernández, L. Hervás[17], L. Labarga, J. del Peso, J. Puga, J. Terrón, J.F. de Trocóniz
*Univer. Autónoma Madrid, Depto de Física Teórica, Madrid, Spain* [n]

F. Corriveau, D.S. Hanna, J. Hartmann, W.N. Murray, A. Ochs, M. Riveline, D.G. Stairs, M. St-Laurent
*McGill University, Dept. of Physics, Montréal, Québec, Canada* [a], [b]

T. Tsurugai
*Meiji Gakuin University, Faculty of General Education, Yokohama, Japan*

V. Bashkirov, B.A. Dolgoshein, A. Stifutkin
*Moscow Engineering Physics Institute, Moscow, Russia* [l]

G.L. Bashindzhagyan, P.F. Ermolov, Yu.A. Golubkov, L.A. Khein, N.A. Korotkova, I.A. Korzhavina, V.A. Kuzmin, O.Yu. Lukina, A.S. Proskuryakov, L.M. Shcheglova[30], A.N. Solomin[30], S.A. Zotkin
*Moscow State University, Institute of Nuclear Physics, Moscow, Russia* [m]

C. Bokel, M. Botje, N. Brümmer, J. Engelen, E. Koffeman, P. Kooijman, A. van Sighem, H. Tiecke, N. Tuning, W. Verkerke, J. Vossebeld, L. Wiggers, E. de Wolf
*NIKHEF and University of Amsterdam, Amsterdam, Netherlands* [i]

D. Acosta[31], B. Bylsma, L.S. Durkin, J. Gilmore, C.M. Ginsburg, C.L. Kim, T.Y. Ling, P. Nylander, T.A. Romanowski[32]
*Ohio State University, Physics Department, Columbus, Ohio, USA* [p]

H.E. Blaikley, R.J. Cashmore, A.M. Cooper-Sarkar, R.C.E. Devenish, J.K. Edmonds, J. Große-Knetter[33], N. Harnew, C. Nath, V.A. Noyes[34], A. Quadt, O. Ruske, J.R. Tickner[35], R. Walczak, D.S. Waters
*Department of Physics, University of Oxford, Oxford, U.K.* [o]

A. Bertolin, R. Brugnera, R. Carlin, F. Dal Corso, U. Dosselli, S. Limentani, M. Morandin, M. Posocco, L. Stanco, R. Stroili, C. Voci
*Dipartimento di Fisica dell' Università and INFN, Padova, Italy* [f]

B.Y. Oh, J.R. Okrasiński, W.S. Toothacker, J.J. Whitmore
*Pennsylvania State University, Dept. of Physics, University Park, PA, USA* [q]

Y. Iga
*Polytechnic University, Sagamihara, Japan* [g]

G. D'Agostini, G. Marini, A. Nigro, M. Raso
*Dipartimento di Fisica, Univ. 'La Sapienza' and INFN, Rome, Italy* [f]

J.C. Hart, N.A. McCubbin, T.P. Shah
*Rutherford Appleton Laboratory, Chilton, Didcot, Oxon, U.K.* [o]

D. Epperson, C. Heusch, J.T. Rahn, H.F.-W. Sadrozinski, A. Seiden, R. Wichmann, D.C. Williams
*University of California, Santa Cruz, CA, USA* [p]

H. Abramowicz[36], G. Briskin[37], S. Dagan[38], S. Kananov[38], A. Levy[38]
*Raymond and Beverly Sackler Faculty of Exact Sciences, School of Physics, Tel-Aviv University,*
*Tel-Aviv, Israel* [e]

T. Abe, T. Fusayasu, M. Inuzuka, K. Nagano, K. Umemori, T. Yamashita
*Department of Physics, University of Tokyo, Tokyo, Japan* [g]

R. Hamatsu, T. Hirose, K. Homma[39], S. Kitamura[40], T. Matsushita, T. Nishimura
*Tokyo Metropolitan University, Dept. of Physics, Tokyo, Japan* [g]

M. Arneodo[20], R. Cirio, M. Costa, M.I. Ferrero, S. Maselli, V. Monaco, C. Peroni, M.C. Petrucci, M. Ruspa, R. Sacchi, A. Solano, A. Staiano
*Università di Torino, Dipartimento di Fisica Sperimentale and INFN, Torino, Italy* [f]

M. Dardo
*II Faculty of Sciences, Torino University and INFN - Alessandria, Italy* [f]

D.C. Bailey, C.-P. Fagerstroem, R. Galea, K.K. Joo, G.M. Levman, J.F. Martin R.S. Orr, S. Polenz, A. Sabetfakhri, D. Simmons
*University of Toronto, Dept. of Physics, Toronto, Ont., Canada* [a]

J.M. Butterworth, C.D. Catterall, M.E. Hayes, E.A. Heaphy, T.W. Jones, J.B. Lane, R.L. Saunders, M.R. Sutton, M. Wing
*University College London, Physics and Astronomy Dept., London, U.K.* [o]

J. Ciborowski, G. Grzelak[41], R.J. Nowak, J.M. Pawlak, R. Pawlak, B. Smalska, T. Tymieniecka, A.K. Wróblewski, J.A. Zakrzewski, A.F. Żarnecki
*Warsaw University, Institute of Experimental Physics, Warsaw, Poland* [j]

M. Adamus
*Institute for Nuclear Studies, Warsaw, Poland* [j]

O. Deppe, Y. Eisenberg[38], D. Hochman, U. Karshon[38]
*Weizmann Institute, Department of Particle Physics, Rehovot, Israel* [d]

W.F. Badgett, D. Chapin, R. Cross, S. Dasu, C. Foudas, R.J. Loveless, S. Mattingly, D.D. Reeder, W.H. Smith, A. Vaiciulis, M. Wodarczyk
*University of Wisconsin, Dept. of Physics, Madison, WI, USA* [p]

A. Deshpande, S. Dhawan, V.W. Hughes
*Yale University, Department of Physics, New Haven, CT, USA* [p]

S. Bhadra, W.R. Frisken, M. Khakzad, W.B. Schmidke
*York University, Dept. of Physics, North York, Ont., Canada* [a]

[1] also at IROE Florence, Italy
[2] now at Univ. of Salerno and INFN Napoli, Italy
[3] supported by Worldlab, Lausanne, Switzerland
[4] now at University of California, Santa Cruz, USA
[5] now at Dongshin University, Naju, Korea
[6] also at DESY
[7] Alfred P. Sloan Foundation Fellow
[8] supported by the Polish State Committee for Scientific Research, grant No. 2P03B14912
[9] now at INFN Bologna
[10] now at Innosoft, Munich, Germany
[11] now at Univ. of Crete, Greece, partially supported by DAAD, Bonn - Kz. A/98/16764
[12] now at Massachusetts Institute of Technology, Cambridge, MA, USA
[13] visitor from Florida State University
[14] supported by European Community Program PRAXIS XXI
[15] now at IFIC, Valencia, Spain
[16] now a self-employed consultant
[17] now at CERN
[18] now at Bayer A.G., Leverkusen, Germany
[19] now at ATLAS Collaboration, Univ. of Munich
[20] also at DESY and Alexander von Humboldt Fellow at University of Hamburg
[21] on leave from MSU, supported by the GIF, contract I-0444-176.07/95
[22] supported by DAAD, Bonn - Kz. A/98/12712
[23] supported by an EC fellowship
[24] PPARC Post-doctoral fellow
[25] now at Applied Materials Inc., Santa Clara
[26] now at Osaka Univ., Osaka, Japan
[27] supported by JSPS Postdoctoral Fellowships for Research Abroad
[28] now at Wayne State University, Detroit
[29] supported by an EC fellowship number ERBFMBICT 972523
[30] partially supported by the Foundation for German-Russian Collaboration DFG-RFBR (grant no. 436 RUS 113/248/3 and no. 436 RUS 113/248/2)
[31] now at University of Florida, Gainesville, FL, USA
[32] now at Department of Energy, Washington
[33] supported by the Feodor Lynen Program of the Alexander von Humboldt foundation
[34] Glasstone Fellow
[35] now at CSIRO, Lucas Heights, Sydney, Australia
[36] an Alexander von Humboldt Fellow at University of Hamburg
[37] now at Brown University, Providence, RI, USA
[38] supported by a MINERVA Fellowship
[39] now at ICEPP, Univ. of Tokyo, Tokyo, Japan
[40] present address: Tokyo Metropolitan College of Allied Medical Sciences, Tokyo 116, Japan
[41] supported by the Polish State Committee for Scientific Research, grant No. 2P03B09308

[a] supported by the Natural Sciences and Engineering Research Council of Canada (NSERC)
[b] supported by the FCAR of Québec, Canada
[c] supported by the German Federal Ministry for Education and Science, Research and Technology (BMBF), under contract numbers 057BN19P, 057FR19P, 057HH19P, 057HH29P
[d] supported by the MINERVA Gesellschaft für Forschung GmbH, the German Israeli Foundation, the U.S.-Israel Binational Science Foundation, and by the Israel Ministry of Science
[e] supported by the German-Israeli Foundation, the Israel Science Foundation, the U.S.-Israel Binational Science Foundation, and by the Israel Ministry of Science
[f] supported by the Italian National Institute for Nuclear Physics (INFN)
[g] supported by the Japanese Ministry of Education, Science and Culture (the Monbusho) and its grants for Scientific Research
[h] supported by the Korean Ministry of Education and Korea Science and Engineering Foundation
[i] supported by the Netherlands Foundation for Research on Matter (FOM)
[j] supported by the Polish State Committee for Scientific Research, grant No. 115/E-343/SPUB/P03/002/97, 2P03B10512, 2P03B10612, 2P03B14212, 2P03B10412
[k] supported by the Polish State Committee for Scientific Research (grant No. 2P03B08614) and Foundation for Polish-German Collaboration
[l] partially supported by the German Federal Ministry for Education and Science, Research and Technology (BMBF)
[m] supported by the Fund for Fundamental Research of Russian Ministry for Science and Education and by the German Federal Ministry for Education and Science, Research and Technology (BMBF)
[n] supported by the Spanish Ministry of Education and Science through funds provided by CICYT
[o] supported by the Particle Physics and Astronomy Research Council
[p] supported by the US Department of Energy
[q] supported by the US National Science Foundation

# 1 Introduction

In photoproduction processes at HERA, a quasi-real photon ($Q^2 \simeq 0$) is emitted by the incoming electron or positron, and interacts with the proton. Such a photon has a hadronic component, which can be assigned a partonic structure. At leading order (LO) in QCD, two types of process take part in photoproduction: direct photon processes, where the photon couples as a point-like particle to a parton from the proton, and resolved photon processes, where one of the partons in the photon scatters on a parton in the proton. The light quark structure of the photon has been extensively studied in photon-photon collisions at $e^+e^-$ storage rings [1], whilst there is little information at present on the charm content of the photon. HERA jet studies have shown some sensitivity to the gluon content of the photon [2, 3], which is still poorly known. In this paper we present a study of charm photoproduction. Here, the direct process is photon-gluon fusion, $\gamma g \to c\bar{c}$, while charm quarks in the parton distributions of the photon and the proton can lead to processes of the type $cg \to cg$, known as charm flavour excitation.

The photoproduction of heavy quarks such as charm can be calculated using perturbative QCD (pQCD) with a hard scale given by the heavy quark mass or by the high transverse momentum of the produced partons. Two types of QCD NLO calculations are available for comparison with measurements of charm photoproduction. The massive charm approach [4] assumes that gluons and light quarks (u,d,s) are the only active partons within the proton and the photon, so that charm is only produced dynamically in the hard process. In the massless charm approach [5, 6, 7] charm is treated as an additional active flavour. The massive approach is expected to be superior for $p_\perp^2 \simeq m_c^2$ while the massless one is expected to describe the data better for $p_\perp^2 \gg m_c^2$ [8], where $p_\perp$ and $m_c$ are the transverse momentum and mass of the charm quark. In NLO calculations, direct and resolved components cannot be unambiguously separated. The massless charm calculations take into account charm excitation processes and thus predict, for a given factorisation scale, a larger resolved component in comparison with the massive calculation. Therefore, it is interesting to compare the predictions of these models to data and to investigate the sensitivity of the experimental results to the partonic content of the photon and specifically to the charm excitation contribution.

In the analysis described in this paper, charm was tagged by identifying $D^{*\pm}(2010)$ mesons in the final state via the charged products of their decay. $D^*$ mesons are reconstructed through the two decay modes[1]:

$$D^{*+} \;\to\; D^0\,\pi_S^+ \to\; (K^-\;\pi^+)\,\pi_S^+, \tag{1}$$

$$D^{*+} \;\to\; D^0\,\pi_S^+ \to\; (K^-\;\pi^+\;\pi^+\;\pi^-)\,\pi_S^+. \tag{2}$$

The small mass difference $\Delta M = M(D^*) - M(D^0) = 145.42 \pm 0.05\,\mathrm{MeV}$ [9] yields a low momentum pion ("soft pion", $\pi_S$) from the $D^*$ decay and prominent signals just above the threshold of the $M(K\pi\pi_S) - M(K\pi)$ and $M(K\pi\pi\pi\pi_S) - M(K\pi\pi\pi)$ distributions, where the phase space contribution is highly suppressed [10].

[1] In this analysis $D^{*\pm}(2010)$ are referred to as $D^*$ and the charge conjugated processes are also included.

We present measurements of integrated and differential cross sections for $D^*$ mesons produced in restricted kinematic regions in $p_\perp^{D^*}$ and $\eta^{D^*}$. Here $\eta^{D^*}$ is the pseudorapidity of the $D^*$, defined as $-\ln(\tan(\theta/2))$, where the polar angle $\theta$ is taken with respect to the proton beam direction.[2] The data sample is larger by more than an order of magnitude compared to our previous study [11], which allows an accurate measurement of the differential cross sections in both $p_\perp^{D^*}$ and $\eta^{D^*}$ and thus a more stringent test of the NLO QCD predictions.

The improved statistics of the $D^*$ sample allows, for the first time, the study of dijet photoproduction in association with charm. In such events, the fraction $x_\gamma^{\rm OBS}$ of the photon momentum which participates in the dijet production can be measured [3]. This quantity is sensitive to the relative contributions of resolved and direct processes [12]. In LO QCD direct photon events at the parton level have $x_\gamma^{\rm OBS}$=1, while resolved photon events populate low values of $x_\gamma^{\rm OBS}$.

# 2 Experimental Conditions

The data presented in this analysis were collected with the ZEUS detector at HERA during the 1996 and 1997 running periods, where a positron beam with energy $E_e$=27.5 GeV collided with a proton beam with energy $E_p$=820 GeV. The data sample corresponds to an integrated luminosity of $36.9 \pm 0.5$ pb$^{-1}$. A detailed description of the ZEUS detector can be found in refs. [13, 14]. Here we present a brief description of the components relevant to the present analysis.

Charged particles are measured by the Central Tracking Detector (CTD) [15] which operates in a magnetic field of 1.43 T provided by a thin superconducting solenoid. The CTD is a drift chamber consisting of 72 cylindrical layers, arranged in 9 superlayers covering the polar angle region $15^\circ < \theta < 164^\circ$. The transverse momentum resolution for full length tracks is $(\sigma_{p_\perp}/p_\perp)^{track} = 0.005 p_\perp^{track} \oplus 0.016$ ($p_\perp^{track}$ in GeV). The CTD was also used to establish an interaction vertex for each event.

Surrounding the solenoid is the uranium-scintillator sampling calorimeter (CAL) [16]. The CAL is hermetic and consists of 5918 cells each read out by two photomultiplier tubes. Under test beam conditions, the CAL has an energy resolution of $0.18/\sqrt{E}$ for electrons and $0.35/\sqrt{E}$ for hadrons ($E$ in GeV). The effects of uranium noise were minimised by discarding cells in the inner (electromagnetic) or outer (hadronic) sections if they had energy deposits of less than 60 (110) MeV. For cells without energy deposits in neighbouring cells this cut was increased to 80 (140) MeV.

The luminosity was measured from the rate of the bremsstrahlung process $e^+p \to e^+\gamma p$, where the photon is measured by a calorimeter [17] located at $Z = -107$ m in the HERA tunnel.

[2] We use the standard ZEUS right-handed coordinate system, in which $X = Y = Z = 0$ is the nominal interaction point and the positive $Z$-axis points in the direction of the proton beam (referred to as the forward direction).

The ZEUS detector uses a three level trigger system [14]. At the first level trigger (FLT) the calorimeter cells were combined to define regional and global sums which were required to exceed various CAL energy thresholds. In addition, at least one CTD track coming from the $ep$ interaction region was required.

At the second level trigger, beam-gas events were rejected by exploiting the excellent timing resolution of the calorimeter and by cutting on the quantity $\Sigma_i(E-p_Z)_i > 8$ GeV, where the sum runs over all calorimeter cells and $p_Z$ is the $Z$ component of the momentum vector assigned to each cell of energy $E$. In addition, events were rejected if the vertex determined by the CTD was not compatible with the nominal $ep$ interaction point.

At the third level trigger (TLT) the full event information was available. Calorimeter timing cuts were tightened in order to reject the remaining beam-gas events. At least one combination of tracks detected in the CTD was required to be within wide mass windows around the nominal values in $\Delta M$ and in $M(K\pi)$ ($M(K\pi\pi\pi)$) for reaction (1) (reaction (2)). In addition, cuts were made on the transverse momenta of tracks associated with these $D^*$ candidates and $p_\perp^{D^*}$ was required to be above 1.8 GeV for reaction (1) and above 3.3 GeV for reaction (2). For the measurement of $D^*$ in association with jets, an alternative trigger strategy is possible at the TLT, based upon the jets themselves. The jet reconstruction algorithm used the CAL cell energies and positions to identify jets. Events were required to have at least two jets, each of which has a transverse energy $E_{T,cal}^{jet} > 4$ GeV and pseudorapidity $\eta^{jet} < 2.5$. This strategy is used as a cross-check for the results on dijets in association with charm.

# 3 Analysis

## 3.1 Offline Data Selection

The event sample was processed using the standard offline ZEUS detector calibration and event reconstruction code. To define an inclusive photoproduction sample, the following requirements were imposed:

- A reconstructed vertex with at least three associated tracks.
- No scattered positron found in the CAL by the algorithm described in ref. [12]. This requirement removes neutral current deep inelastic scattering (DIS) events, thereby restricting $Q^2$ to below $\simeq 1\,\mathrm{GeV}^2$. The corresponding median $Q^2$ in our photoproduction sample is estimated from Monte Carlo (MC) simulations to be $\simeq 3{\cdot}10^{-4}\,\mathrm{GeV}^2$.
- $115 < W_{JB} < 250$ GeV, where $W_{JB} = \sqrt{4y_{JB}E_pE_e}$. Here $W_{JB}$ and $y_{JB} = \Sigma_i(E-p_Z)_i/2E_e$ are the Jacquet-Blondel [18] estimators of $W$ and $y$, respectively, and $y$ is the fraction of the positron beam energy taken by the photon.

The value of $W_{JB}$ was determined from the energy deposits in the uranium calorimeter. The lower $W_{JB}$ cut rejects events from a region where the acceptance is small because of the trigger requirements. The upper cut rejects possible background from DIS events in which the scattered positron had not been recognised. A systematic shift in the reconstructed values of $W_{JB}$ with respect to the true $W$ of the event, due to energy losses in inactive material in front of the calorimeter and particles lost in the beam pipe, was corrected [12, 19], using the MC simulation of the detector described in section 4. The centre of mass energy range covered by the photoproduction sample is then $130 < W < 280\,\mathrm{GeV}$, corresponding to $0.19 < y < 0.87$.

## 3.2 Reconstruction of $D^*$ Candidates

A $D^*$ reconstruction algorithm was applied to all selected events. It uses the mass difference technique to suppress the high background due to random combinations from non-charm events, which have a much higher cross section. Only tracks associated with the event vertex and having $p_\perp^{track} > 0.15\,\mathrm{GeV}$ and $|\eta^{track}| < 1.75$ were included in the combinations.

Reconstructed tracks in each event were combined to form $D^0$ candidates assuming the decay channels (1) or (2). For both cases, $D^0$ candidates were formed by calculating the invariant mass $M(K\pi)$ or $M(K\pi\pi\pi)$ for combinations having a total charge of zero. No particle identification was used, so kaon and pion masses were assigned in turn to each particle in the combination. Transverse momenta of $p_\perp^{track} > 0.5\,\mathrm{GeV}$ were required for all tracks of channel (1) and for the track taken to be the kaon for channel (2). Pion candidates in the latter channel were required to have $p_\perp^{track} > 0.3\,\mathrm{GeV}$. An additional track, assumed to be the soft pion, $\pi_S$, with a charge opposite to that of the particle taken as a kaon, was then added to the $D^0$ candidate. The mass difference $\Delta M = M(K\pi\pi_S) - M(K\pi)$ for channel (1) or $M(K\pi\pi\pi\pi_S) - M(K\pi\pi\pi)$ for channel (2) was evaluated. The reconstructed $D^*$ candidates were required to be in the pseudorapidity range $-1.5 < \eta^{D^*} < 1.5$ , for which the CTD acceptance is high.

To comply with the $p_\perp^{D^*}$ cut applied at the TLT, we required $p_\perp^{K\pi\pi_S} > 2\,\mathrm{GeV}$ for channel (1). The number of decay particles in channel (2) is larger: to improve the signal to background ratio, we required $p_\perp^{K\pi\pi\pi\pi_S} > 4\,\mathrm{GeV}$ for this channel. Since more combinatorial background exists in the forward direction as well as in the region of low $p_\perp^{D^*}$, an additional cut, $p_\perp^{D^*}/E_\perp^{\theta>10^\circ} > 0.1$, was applied to both channels. Here $E_\perp^{\theta>10^\circ}$ is the transverse energy outside a cone of $\theta = 10^\circ$ defined with respect to the proton direction. This cut, as verified by MC studies, removed a significant fraction of the background whilst preserving 99% of the $D^*$ signal.

The $\Delta M$ distributions of channel (1) and channel (2) for combinations with $M(K\pi)$ or $M(K\pi\pi\pi)$ between 1.80 and 1.92 GeV are shown in Fig.1. Clear peaks at the nominal value of $M(D^*) - M(D^0)$ are evident. MC studies have shown that the contribution of other $D^0$ decay modes to the $\Delta M$ peak is small and can be neglected.

The $\Delta M$ signals were fitted, using a maximum likelihood method, to a sum of a Gaussian (describing the signal) and a functional form (describing the background shape) of $A \cdot (\Delta M - m_\pi)^B$. The mass values obtained were $\Delta M = 145.45 \pm 0.02$ $(stat.)$ MeV for channel (1) and $145.42 \pm 0.05$ $(stat.)$ MeV for channel (2), in agreement with the PDG value [9]. The width of the signals were $\sigma = 0.68 \pm 0.02$ MeV and $\sigma = 0.72 \pm 0.05$ MeV, respectively, in agreement with our MC simulation.

To determine the background under the peak for channel (1), combinations in the same $M(K\pi)$ range, in which both tracks forming the $D^0$ candidates have the same charge, with $\pi_S$ having the opposite charge, were used. These are referred to as wrong charge combinations. The $\Delta M$ distribution from such combinations is shown as the dashed histogram in Fig. 1a. The inset to Fig. 1a shows the $M(K\pi)$ distribution from combinations having a mass difference in the range $143 < \Delta M < 148$ MeV. A $D^0$ peak is clearly observed. The dashed histogram shows the wrong charge combinations defined above. The excess of events with respect to the wrong charge distribution below the $D^0$ region originates mostly from $D^0$ decays involving neutral pions [11]. The number of reconstructed $D^*$ mesons in channel (1) was determined by subtracting the wrong charge distribution after normalising it to the right charge distribution in the range $150 < \Delta M < 170$ MeV. After subtracting the background from the $\Delta M$ distribution of Fig. 1a, a signal of $3702 \pm 136$ $D^*$ events was obtained for $p_\perp^{D^*} > 2$ GeV.

Side band subtraction, close to the signal region, was used to estimate the background under the $\Delta M$ signal of channel (2). The side bands, $1.70 < M(K\pi\pi\pi) < 1.80$ GeV and $1.92 < M(K\pi\pi\pi) < 2.02$ GeV, were normalised to the region $148 < \Delta M < 165$ MeV (dashed histogram in Fig. 1b). This subtraction removed the combinatorial background coming from events or tracks in which no $D^*$ decaying through this channel is produced, and part of the background due to the mass misassignment of the kaon and pion candidates with the same charge from the $D^0$ decay. The remaining background, coming from the mass misassignment, is reproduced in the MC acceptance calculations. The inset to Fig. 1b shows the $M(K\pi\pi\pi)$ distribution from combinations having a mass difference in the range $143 < \Delta M < 148$ MeV. A $D^0$ peak is clearly observed. The total number of $D^*$ mesons in channel (2) extracted for $p_\perp^{D^*} > 4$ GeV from the $\Delta M$ distribution with the side band subtraction was $1397 \pm 108$.

## 3.3 Jet Reconstruction

For the measurement of charmed dijet events, the KTCLUS cluster algorithm [20] has been implemented in its "inclusive" mode [21]. In this algorithm, jets are unambiguously defined at the hadron, parton and CAL levels. Using the $p_T$ recombination scheme [21], the parameters of the jets are calculated as: $E_T^{jet} = \sum_i E_{T_i}$; $\eta^{jet} = (1/E_T^{jet})(\sum_i E_{T_i}\eta_i)$; $\phi^{jet} = (1/E_T^{jet})(\sum_i E_{T_i}\phi_i)$. The sums run over all calorimeter cells, hadrons or partons belonging to the corresponding jet. Here $E_{T_i}$, $\eta_i$ and $\phi_i$ are the transverse energy, pseudorapidity and azimuthal angle.

For the analysis of charm with associated dijets, events containing a $D^*$ meson in chan-

nel (1) with $p_\perp^{K\pi\pi_S} > 3$ GeV were used. The events were also required to have at least two jets with $|\eta^{jet}| < 2.4$ and a reconstructed $E_{T,cal}^{jet} > 5$ GeV. With this selection, $587 \pm 41$ events were found after subtraction of the wrong charge background. In addition, an analysis with $E_{T,cal}^{jet} > 4$ GeV was performed, yielding $971 \pm 52$ events. The distribution of the distance between a $D^*$ candidate and the jet closest to it in the $\eta^{jet}$- $\phi^{jet}$ space shows that the measured $D^*$ belongs to one of the two jets. In more than 80% of the cases, this distance was less than 0.2, which is consistent with the observed hard fragmentation of heavy quarks [22].

# 4 Monte Carlo Simulation

The MC programs PYTHIA 6.1 [23] and HERWIG 5.9 [24] were used to model the hadronic final states in charm production and to study the efficiency of the cuts used in the data selection. Both programs are general purpose generators including a wide range of photoproduction processes.

Large samples of charm events were generated for channels (1) and (2) using both MC programs. Direct and resolved photon events, including charm excitation, were generated using as a reference sample the MRSG [25] parametrisation for the proton and GRV- G HO [26] for the photon. These samples have at least ten times the statistics of the data, so their contribution to the statistical error is negligible. To check the sensitivity of the results to the choice of the structure function, the reference samples were reweighted to simulate other parton distributions of both the proton and the photon. The MC studies showed that, in the kinematic range used here, the results are insensitive to contributions from charm excitation in the proton.

In order to include photoproduced $D^*$ mesons originating from $b$ quark events, a sample of such events was generated with a ratio to the charm sample proportional to the cross section ratio of the two processes used in the MC ($\simeq 1 : 100$). Within the kinematic range of the inclusive $D^*$ analysis, the contribution of $b$ quark production to the $D^*$ cross section is estimated to be $\simeq 5\%$. For the kinematic range of dijets in association with charm the corresponding estimate is $\simeq 10\%$.

Events containing at least one $D^*$ decaying into channel (1) or (2) were processed through the standard ZEUS detector and trigger simulation programs and through the same event reconstruction package used for offline data processing. Tracks were reconstructed both in the TLT and the offline simulations. The MC efficiency of the tracking trigger was checked using the jet trigger described in section 2 and found to be consistent with the data. Satisfactory agreement was observed between the CTD transverse momentum resolution in the MC samples and the data.

An additional sample of events was generated using multiparton interactions (MI) in HERWIG [27] as an attempt to simulate the energy from additional softer scatters ("underlying event").

# 5 Measurement of Inclusive $D^*$ Cross Sections

The improved trigger and detector conditions compared to that used for our previous results [11] allow measurements of the inclusive $ep \rightarrow D^*X$ cross sections in a wider kinematic region: $p_\perp^{D^*} > 2\,\mathrm{GeV}$ and $-1.5 < \eta^{D^*} < 1.5$. The integrated $D^*$ cross section in the above region for $Q^2 < 1\,\mathrm{GeV}^2$, $130 < W < 280\,\mathrm{GeV}$ was calculated using the formula $\sigma_{ep\rightarrow D^*X} = N_{corr}^{D^*}/\mathcal{L}B$, where $N_{corr}^{D^*}$ is the acceptance-corrected number of $D^*$, $B$ is the combined $D^*$ and $D^0$ decay branching ratios ($0.0262 \pm 0.0010$ for channel (1) and $0.051 \pm 0.003$ for channel (2)) [9] and $\mathcal{L}= 36.9 \pm 0.5$ pb$^{-1}$ is the integrated luminosity.

In order to obtain $N_{corr}^{D^*}$, a correction factor $\omega_i$, defined as the number of generated divided by the number of reconstructed $D^*$ mesons, was calculated for channel (1) from the MC simulation using a three-dimensional grid in the quantities $p_\perp^{D^*}$, $\eta^{D^*}$ and $W_{JB}$. The index $i$ corresponds to a given grid bin. All $D^*$ data candidates in a grid bin were corrected by the appropriate $\omega_i$, yielding $N_{corr}^{D^*} = \Sigma_i \omega_i (N_{rec}^{D^*})_i$. Here $(N_{rec}^{D^*})_i$ is the number of reconstructed $D^*$ candidates in bin $i$. For channel (2) a one dimensional bin-by-bin unfolding procedure was used.

The reference MC used to calculate the acceptance for channel (1) was HERWIG. For channel (2) PYTHIA was used, since HERWIG does not reproduce the decay widths of resonances which contribute to the $K\pi\pi\pi$ final state [9]. Results obtained from the alternative MC were used in each channel to estimate the systematic uncertainties.

Table 1 summarises the results for $N_{rec}^{D^*}$ after background subtraction and the integrated cross sections for both decay channels with various $p_\perp^{D^*}$ cuts. The first error is statistical and the second is the combined systematic uncertainty. The overall scale uncertainties ($\pm 1.4\%$ from the luminosity measurement, and $\pm 3.7\%$ or $\pm 5.7\%$ from the branching ratios [9] of channels (1) or (2) respectively) were not included in the combined systematic errors.

The differential cross sections $d\sigma/dp_\perp^{D^*}$ and $d\sigma/d\eta^{D^*}$ were measured using the same procedure. The combinatorial background was subtracted bin-by-bin from each distribution using the methods described above. The $d\sigma/dp_\perp^{D^*}$ distribution is shown in Fig. 2 for $-1.5 < \eta^{D^*} < 1.5$ for channels (1) all and (2) and listed in Table 2 for channel (1). The $d\sigma/d\eta^{D^*}$ distributions for $p_\perp^{D^*} > 2$ and 3 GeV for channel (1) are shown in Fig. 3(a,b) and for $p_\perp^{D^*} > 4$ and 6 GeV for both channels in Fig. 3(c,d). In Table 3 the $d\sigma/d\eta^{D^*}$ values are listed for channel (1).

The results from the two $D^0$ decay modes are in good agreement and are consistent with our published measurements based on data taken in 1994 [11].

## 5.1 Systematic Uncertainties

A detailed study of possible sources of systematic uncertainties was carried out for all the measured cross sections. The numbers quoted below are for the integrated cross section with $p_\perp^{D^*} > 2\,\mathrm{GeV}$ of channel (1), unless stated otherwise.

| | $p_\perp^{D^*} > 2$ GeV | $p_\perp^{D^*} > 3$ GeV | $p_\perp^{D^*} > 4$ GeV | $p_\perp^{D^*} > 6$ GeV |
|---|---|---|---|---|
| $N_{\rm rec}^{D^*}(K\pi\pi_{\rm s})$ | $3702 \pm 136$ | $2619 \pm 82$ | $1505 \pm 50$ | $410 \pm 24$ |
| $N_{\rm rec}^{D^*}(K\pi\pi\pi\pi_{\rm s})$ | | | $1397 \pm 108$ | $411 \pm 40$ |
| $\sigma_{\rm data}(K\pi\pi_{\rm s})$ [nb] | $18.9 \pm 1.2\,^{+1.8}_{-0.8}$ | $9.17 \pm 0.35\,^{+0.40}_{-0.39}$ | $4.24 \pm 0.16\,^{+0.16}_{-0.14}$ | $0.948 \pm 0.061\,^{+0.046}_{-0.047}$ |
| $\sigma_{\rm data}(K\pi\pi\pi\pi_{\rm s})$ [nb] | | | $4.22 \pm 0.33\,^{+0.41}_{-0.15}$ | $0.991 \pm 0.098\,^{+0.099}_{-0.063}$ |
| $\sigma_{\rm massive}$ [nb] | 13.1 | 5.43 | 2.46 | 0.665 |
| $\sigma_{\rm massless}$ [5] [nb] | 25.3 | 8.50 | 3.37 | 0.739 |
| $\sigma_{\rm massless}$ [7] [nb] | 17.4 | 5.83 | 2.34 | 0.520 |

Table 1: Number of reconstructed $D^*$ mesons after background subtraction and integrated cross sections, $\sigma_{ep\to D^*X}$, for $Q^2 < 1$ GeV$^2$, $130 < W < 280$ GeV, $-1.5 < \eta^{D^*} < 1.5$ and various $p_\perp^{D^*}$ cuts. Predictions of the NLO QCD calculations are given for the reference parameters and parton density functions (see section 6). The first error is statistical and the second is systematic. Overall normalisation uncertainties due to luminosity measurement ($\pm 1.4\%$) and to $D^*$ and $D^0$ decay branching ratios ($\pm 3.7\%$ for channel (1) and $\pm 5.7\%$ for channel (2)) are not included in the systematic errors.

- Uncertainties originating from the modelling of the MC simulation were estimated from the difference in the cross sections obtained with the two event generators PYTHIA and HERWIG. They are negligible for the cross section with $p_\perp^{D^*} > 2$ GeV; however they vary between $-2.2\%$ and $-4.5\%$ for the higher $p_\perp^{D^*}$ cuts.

- To estimate the uncertainties in the tracking procedure, the track selection cuts were varied by $\pm 10\%$ from the nominal values (section 3.2). The resulting combined uncertainty in the cross section is $^{+7.1}_{-2.2}\%$. Changing the $p_\perp^{D^*}/E_\perp^{\theta>10^\circ}$ cut by the same amount yields an uncertainty of $^{+0.8}_{-0.4}\%$.

- The MC simulation was found to reproduce the absolute energy scale of the CAL to within $\pm 3\%$ [28]. A shift of $\pm 3\%$ due to the CAL energy scale uncertainty produces a variation of $^{+3.4}_{-2.6}\%$ in the cross section. The dominant source of this uncertainty is due to the acceptance of the CAL energy thresholds in the FLT (section 2). An additional uncertainty due to a small mismatch between data and MC in the observed CAL energy distribution amounts to $^{+1.5}_{-1.2}\%$.

- Uncertainties in the background estimation of $^{+2.8}_{-0.4}\%$ were obtained by varying the $\Delta M$ and $M(D^0)$ mass windows and the normalisation region (section 3.2).

- The uncertainty from correcting $W_{JB}$ to the true $W$, determined by moving the $W_{JB}$ boundary values by the estimated resolution of $\pm 7\%$, was negligible for the cross section with $p_\perp^{D^*} > 2$ GeV. For higher $p_\perp^{D^*}$ cuts the uncertainty varies between $-1.7\%$ and $+1.5\%$.

- Reweighting the reference MC samples to other parton density parametrisations [29] for the proton (MRSA′, GRV94HO, CTEQ3M) gave a variation of $^{+0.0}_{-1.5}\%$ in the cross

| $p_\perp^{D^*}$ (range) GeV | $d\sigma/dp_\perp^{D^*}$ (nb/GeV) |
|---|---|
| 2.458 ( 2 – 3 ) | $9.68 \pm 1.16\ ^{+1.55}_{-0.56}$ |
| 3.464 ( 3 – 4 ) | $4.94 \pm 0.31\ ^{+0.30}_{-0.31}$ |
| 4.469 ( 4 – 5 ) | $2.22 \pm 0.13\ ^{+0.10}_{-0.11}$ |
| 5.470 ( 5 – 6 ) | $1.076 \pm 0.073\ ^{+0.071}_{-0.043}$ |
| 6.902 ( 6 – 8 ) | $0.328 \pm 0.024\ ^{+0.020}_{-0.013}$ |
| 9.672 ( 8 –12 ) | $0.067 \pm 0.008\ ^{+0.004}_{-0.006}$ |

Table 2: The differential cross section $d\sigma/dp_\perp^{D^*}$ for channel (1) as function of $p_\perp^{D^*}$ for the kinematic region of Fig.2. The $p_\perp^{D^*}$ points are given at the positions of the average values of an exponential fit in each bin. The $p_\perp^{D^*}$ range is given in brackets. The first error is statistical and the second is systematic. Overall normalisation uncertainties due to luminosity measurement ($\pm 1.4\%$) and to $D^*$ and $D^0$ decay branching ratios ($\pm 3.7\%$) are not included in the systematic errors.

| $\eta^{D^*}$ range | $d\sigma/d\eta^{D^*}$ (nb) | |
|---|---|---|
| | $p_\perp^{D^*} > 2\,\mathrm{GeV}$ | $p_\perp^{D^*} > 3\,\mathrm{GeV}$ |
| $(-1.5, -1.0)$ | $8.89 \pm 0.81\ ^{+0.89}_{-0.33}$ | $2.96 \pm 0.23\ ^{+0.24}_{-0.26}$ |
| $(-1.0, -0.5)$ | $8.16 \pm 0.80\ ^{+0.70}_{-0.48}$ | $4.17 \pm 0.29\ ^{+0.15}_{-0.26}$ |
| $(-0.5,\ 0.0)$ | $7.61 \pm 0.79\ ^{+0.97}_{-0.48}$ | $3.88 \pm 0.28\ ^{+0.25}_{-0.18}$ |
| $(\ 0.0,\ 0.5)$ | $5.23 \pm 0.99\ ^{+1.09}_{-0.55}$ | $2.93 \pm 0.28\ ^{+0.18}_{-0.25}$ |
| $(\ 0.5,\ 1.0)$ | $3.21 \pm 1.02\ ^{+0.86}_{-0.66}$ | $2.11 \pm 0.28\ ^{+0.19}_{-0.21}$ |
| $(\ 1.0,\ 1.5)$ | $4.65 \pm 1.40\ ^{+1.49}_{-1.06}$ | $2.32 \pm 0.34\ ^{+0.46}_{-0.37}$ |
| | $p_\perp^{D^*} > 4\,\mathrm{GeV}$ | $p_\perp^{D^*} > 6\,\mathrm{GeV}$ |
| $(-1.5, -1.0)$ | $1.021 \pm 0.096\ ^{+0.079}_{-0.095}$ | $0.052 \pm 0.052\ ^{+0.048}_{-0.037}$ |
| $(-1.0, -0.5)$ | $1.641 \pm 0.137\ ^{+0.074}_{-0.118}$ | $0.331 \pm 0.047\ ^{+0.054}_{-0.054}$ |
| $(-0.5,\ 0.0)$ | $1.877 \pm 0.143\ ^{+0.117}_{-0.112}$ | $0.460 \pm 0.061\ ^{+0.031}_{-0.039}$ |
| $(\ 0.0,\ 0.5)$ | $1.662 \pm 0.137\ ^{+0.077}_{-0.067}$ | $0.398 \pm 0.056\ ^{+0.032}_{-0.028}$ |
| $(\ 0.5,\ 1.0)$ | $1.090 \pm 0.117\ ^{+0.138}_{-0.079}$ | $0.374 \pm 0.045\ ^{+0.029}_{-0.036}$ |
| $(\ 1.0,\ 1.5)$ | $1.186 \pm 0.142\ ^{+0.132}_{-0.137}$ | $0.242 \pm 0.062\ ^{+0.030}_{-0.043}$ |

Table 3: The differential cross sections $d\sigma/d\eta^{D^*}$ for channel (1) as function of $\eta^{D^*}$ for the kinematic regions of Fig.3. The $\eta^{D^*}$ range is given in brackets. The quoted cross sections correspond to the centres of the corresponding bins. The first error is statistical and the second is systematic. Overall normalisation uncertainties due to luminosity measurement ($\pm 1.4\%$)and to $D^*$ and $D^0$ decay branching ratios ($\pm 3.7\%$) are not included in the systematic errors.

section. Since the photon structure is not well known, we used several parton density parametrisations (LAC-G1, ACFGP, GS-G HO) and in addition we allowed a $\pm 10\%$ variation of the ratio of resolved to direct photon contributions with respect to the reference structure function. The largest resulting uncertainty in the cross section was $^{+4.1}_{-0.6}\%$.

All contributions to the systematic uncertainties, except the overall scale uncertainties, were added in quadrature. The combined systematic uncertainties in the cross sections are given in Table 1. For the differential cross sections the systematic errors were added in quadrature to the statistical and are indicated in Figs. 2-4 by the outer error bars. In Tables 2 and 3 both types of errors are given separately.

# 6 Comparison with NLO QCD Calculations

## 6.1 Massive Charm Scheme

Full NLO calculations in the massive charm scheme of total and differential cross sections for heavy quark production in the HERA kinematic region have been published in ref. [4]. The computation was done as in ref. [11] for $\gamma p \to c\bar{c}X$ [30] and then converted to $ep \to c\bar{c}X$ cross section with the appropriate flux factors [19]. The fraction of $c$ quarks fragmenting into a $D^{*+}$ as measured by the OPAL collaboration [31], $0.222 \pm 0.014 \pm 0.014$, was used to produce total and differential $D^*$ cross sections in the restricted kinematic regions of our measurements.

The calculation used the MRSG [25] and GRV-G HO [26] parton density parametrisations for the proton and photon, respectively. The renormalisation scale used was $\mu_R = m_\perp = \sqrt{m_c^2 + p_\perp^2}$ ($m_c = 1.5\,\mathrm{GeV}$) and the factorisation scales of the photon and proton structure functions were set to $\mu_F = 2m_\perp$. The charm fragmentation into $D^*$ was performed using the Peterson function [22] $f(z) \propto \left[z\left(1 - 1/z - \epsilon/(1-z)\right)^2\right]^{-1}$. Here $z$ is the fraction of the charm quark momentum taken by the $D^*$ and $\epsilon$ is a free parameter.

The NLO cross sections obtained for the same kinematic regions as the data are listed in Table 1 for $\epsilon$=0.02 and shown in Figs. 2 and 3 for $\epsilon$=0.02 (dashed lines) and $\epsilon$=0.06 (dash-dotted lines). The value $\epsilon$=0.06 is based on ref. [32] and used by Frixione et al. in ref. [4], while $\epsilon$=0.02 is suggested by recent fits to $e^+e^-$ data [7]. The predicted cross sections are considerably lower than those measured. The dotted line, which corresponds to the extreme choice $\mu_R = 0.5 m_\perp$ and $m_c = 1.2$ GeV, is still below the data at the high $\eta^{D^*}$ regions. The calculated shapes in both the $p_\perp^{D^*}$ and $\eta^{D^*}$ distributions are also inconsistent with the data.

The result of applying an effective intrinsic transverse momentum, $k_T$, to the incoming partons in the massive charm scheme [30] is relatively small. The predicted cross sections increase by about 10% with $\langle k_T^2 \rangle = 1$ GeV$^2$, mostly at low $p_T$ and in the backward

direction. In a semi-hard approach [33] this effect was calculated according to the BFKL evolution [34]. Recently LO predictions using this approach have become available [35]. The predicted cross sections for our kinematic range are close to the data in absolute value but do not match the shape of the $\eta^{D^*}$ distribution.

## 6.2 Massless Charm Scheme

A second type of NLO calculation [5, 6, 7], the massless charm scheme, assumes charm to be an active flavour in both the proton and the photon. The two massless charm calculations factorise the perturbative and non-perturbative components of the fragmentation differently and fit the latter part to the Peterson function [22], using recent $e^+e^-$ data on $D^*$ production to extract the $\epsilon$ parameter. The fitted values obtained by the two calculations in their specific factorisation schemes are $\epsilon$=0.116 [5] and $\epsilon$=0.02 [7]. Similar cross sections are obtained in each of the massless charm calculations by fitting fragmentation functions other than the Peterson one to the $e^+e^-$ data. These predictions are expected not to be reliable when the minimum $p_\perp^{D^*}$ cut is as low as 2 GeV.

The cross sections predicted with these calculations [5, 7] for the kinematic region of our measurement are listed in Table 1 and shown as full lines in Figs. 2 and 3. The parton density parametrisations used were CTEQ4M [36] for the proton and GRV-G HO [26] for the photon. The renormalisation and factorisation scales as well as the values of $m_c$ are the same as in the calculation of the massive charm approach.

The predictions of the two massless charm models give similar shapes of the differential cross sections (Figs.2 and 3), but disagree with each other in absolute magnitude by $\simeq$ 40%. The cross sections obtained by these predictions are mostly below the data. In particular the data are above the NLO expectations in the forward direction. The contribution of $D^*$ produced from $b\bar{b}$ in our kinematic region, not included in the NLO curves, is predicted[6] to be below 5%, in agreement with our MC estimation (section 4). This fraction is found from the MC studies to be slightly higher in the forward region, where it is up to 7%.

Using the MRSG [25] parton density parametrisation of the proton has no significant effect on the predictions. In contrast, the calculations depend on the parton density parametrisations of the photon and in particular its charm content. In order to check the sensitivity of the $d\sigma/d\eta^{D^*}$ data to the parton density parametrisation of the photon, we compare the results for $p_\perp^{D^*} > 3$ GeV and $p_\perp^{D^*} > 4$ GeV in Fig. 4 with the two NLO massless charm predictions [5, 7] obtained with the photon parton density parametrisations GRV-G HO [26], GS-G HO [37] and AFG [38]. The differences between the various photon parton densities are at the 20% level or less in the integrated cross sections, but in the differential cross sections considerable differences in shape are observed. For the massless charm scheme of ref. [5], the GS-G HO curves [37] are closest to the data. However, in the GS-G HO parton density function used for this calculation, charm and u-quarks contribute equally.

# 7 Measurement of $D^*$ Dijet Cross Sections

Given the discrepancies observed between data and NLO predictions in the inclusive $D^*$ measurements, it is of interest to study the kinematics of charm production in more detail. The measurement of jets in the final state allows the kinematics of the hard scattering process to be reconstructed. In order to compare the measurement with QCD calculations at any order, we define [39]

$$x_\gamma^{\rm OBS} = \frac{\Sigma_{\rm jets}(E_T^{jet}\ e^{-\eta^{jet}})}{2E_e y}, \tag{3}$$

where $\eta^{jet}$ is the jet pseudorapidity, $y$ is estimated by $y_{JB}$, and the jets in the sum are the two highest $E_T^{jet}$ jets within the accepted $\eta^{jet}$ range. The variable $x_\gamma^{\rm OBS}$ is the fraction of the photon momentum contributing to the production of the two jets with the highest $E_T^{jet}$. In measurements, as well as in MC simulations and higher order calculations, direct and resolved samples can be separated by a cut on $x_\gamma^{\rm OBS}$. In this analysis we define a direct (resolved) photon process by the selection $x_\gamma^{\rm OBS} \geq 0.75 (< 0.75)$.

Fig. 5 shows the uncorrected transverse energy flow, $(1/N_{jet})dE_T/d\Delta\eta$, around the jet axis ("jet profile") as a function of $\Delta\eta = \eta^{CELL} - \eta^{jet}$, the distance in $\eta$ of the CAL cell from the jet axis for the sample of dijet events associated with a $D^*$ (section 3.3) with $E_{T,cal}^{jet} > 4$ GeV. As for the inclusive $D^*$ analysis (section 3.2), wrong charge combinations were used to subtract background from the $E_T$ flow in the $D^*$ signal region. In order to reduce the uncertainties due to the background subtraction procedure, a narrower $D^*$ region was used in the jet profile plots: $1.82 < M(K\pi) < 1.90$ GeV and $0.144 < \Delta M < 0.147$ GeV. The jet sample is divided into three regions of $\eta^{jet}$: $-2.4 < \eta^{jet} < 0.0$, $0.0 < \eta^{jet} < 1.0$ and $1.0 < \eta^{jet} < 2.4$. The distributions are plotted separately for direct ($x_\gamma^{\rm OBS} \geq 0.75$) and resolved ($x_\gamma^{\rm OBS} < 0.75$) events. The jet profiles are compared to the results of the HERWIG MC which includes LO-direct and LO-resolved photon processes [3], shown as the full histogram. In inclusive dijet events [3], the MC simulation gives too little transverse energy in the forward (positive $\Delta\eta$) region for low-$E_T$ jets, even when that simulation includes MI. In contrast, our charm dijet $E_T$ flow distributions are in reasonable accord with the MC without MI, including the forward region.

Also shown in Fig. 5 are the jet profiles obtained if only HERWIG LO-direct photon events are used (dotted histogram). These profiles have reduced $E_T$ flow in the backward (negative $\Delta\eta$) region and do not describe the data with $x_\gamma^{\rm OBS} < 0.75$, in particular for the ranges $0 < \eta^{jet} < 1$ and $1 < \eta^{jet} < 2.4$. The $E_T$ flow in the backward direction is consistent with the presence of a remnant from the resolved photon.

To calculate the cross section $d\sigma/dx_\gamma^{\rm OBS}$ for dijets with an associated $D^*$ meson, MC event samples have been used to correct the charm dijet data for the efficiencies of the trigger and selection cuts and for migrations caused by detector effects. The resolution of the kinematic variables was studied by comparing the MC simulated jets reconstructed from

[3] We distinguish between LO-direct and LO-resolved photon contributions using the LO diagrams as implemented in the MC simulation.

final state particles (hadron jets) with jets reconstructed from the energies measured in the calorimeter (detector jets), and by comparing the corrected $y_{JB}$ with the true $y$. The resolutions obtained are: in $E_T^{jet} \simeq 15\%$, in $\eta^{jet} \simeq 0.1$ and in $x_\gamma^{\rm OBS} \simeq 0.06$. The correction factors are calculated as the ratio $N_{\rm true}/N_{\rm rec}$ in each $x_\gamma^{\rm OBS}$ bin, where $N_{\rm true}$ is the number of events generated in a bin and $N_{\rm rec}$ is the number of events reconstructed in that bin after detector simulation and all experimental cuts.

Differential cross sections in $d\sigma/dx_\gamma^{\rm OBS}$ in the range $130 < W < 280\,{\rm GeV}$ , $Q^2 < 1\ {\rm GeV}^2$ are given for jets with $|\eta^{jet}| < 2.4$, $E_T^{jet1} > 7$ GeV, $E_T^{jet2} > 6$ GeV and at least one $D^*$ in the range $p_\perp^{D^*} > 3$ GeV, $-1.5 < \eta^{D^*} < 1.5$. The asymmetric cut on the hadron level $E_T^{jet}$ values has been applied in order to avoid a problem associated with a singularity in the NLO calculations due to the soft gluons that accompany the jet [40]. The increased minimum $p_\perp^{D^*}$ of 3 GeV compared to the inclusive $D^*$ analysis (section 5) is due to the fact that there is almost no $D^*$ signal in the region below this value due to the requirement of the dijet cuts. Background subtraction was performed as described in section 3.2 for channel (1).

The $d\sigma/dx_\gamma^{\rm OBS}$ results are shown in Fig.6 and listed in Table 4. All uncertainties except that due to the energy scale have been added in quadrature. The systematic uncertainty due to the energy scale is shown in Fig.6 as the shaded band. The cross section integrated over $x_\gamma^{\rm OBS}$ is $1.65 \pm 0.12\ (stat.)^{+0.11}_{-0.06}\ (syst.)\ ^{+0.20}_{-0.16}\ (energy\ scale)$ nb. Results are also presented in Table 4 for the region $E_T^{jet1}$ >6 GeV, $E_T^{jet2}$ >5 GeV, where the cross section integrated over $x_\gamma^{\rm OBS}$ is $2.57 \pm\ 0.14\ (stat.)^{+0.13}_{-0.08}\ (syst.)\ ^{+0.29}_{-0.23}\ (energy\ scale)$ nb.

## 7.1 Systematic Uncertainties

Sources of systematic uncertainties in the cross section measurements were investigated in a similar manner to section 5.1. Additional contributions specific to the $D^*$ and associated dijet sample for the integrated cross sections in $x_\gamma^{\rm OBS}$ with $E_T^{jet1}$ >7 GeV, $E_T^{jet2}$ >6 GeV are:

- The possible shift in the CAL energy scale was increased to $\pm 5\%$ due to the additional uncertainty in the $E_{T,cal}^{jet}$ measurement [3]. The variation in the cross section is $^{+12.2}_{-9.8}\%$.
- The uncertainty due to shifting the minimum $E_{T,cal}^{jet}$ cut by $\pm 1$ GeV, which corresponds to the jet resolution in this low energy region is estimated to be $^{+2.1}_{-0.1}\%$.
- Varying the $\eta^{jet}$ cut values by $\pm 0.1$ yields an uncertainty of $^{+0.1}_{-1.3}\%$.
- Using the HERWIG MC with MI for the acceptance calculations contributes an uncertainty of $+1.1\%$.

All contributions to the systematic errors, excluding luminosity, branching ratios and energy scale uncertainties, were added in quadrature. The final systematic uncertainty in

| $x_\gamma^{\rm OBS}$ range | $d\sigma/dx_\gamma^{\rm OBS}(nb)$ | $d\sigma/dx_\gamma^{\rm OBS}(nb)$ |
|---|---|---|
| | $E_T^{jet1} > 7\,\mathrm{GeV}$ | $E_T^{jet1} > 6\,\mathrm{GeV}$ |
| | $E_T^{jet2} > 6\,\mathrm{GeV}$ | $E_T^{jet2} > 5\,\mathrm{GeV}$ |
| (0.000–0.125) | $0.32 \pm 0.19\,^{+0.14\,+0.00}_{-0.26\,-0.06}$ | $0.42 \pm 0.21\,^{+0.33\,+0.06}_{-0.23\,-0.08}$ |
| (0.125–0.250) | $1.06 \pm 0.30\,^{+0.17\,+0.10}_{-0.22\,-0.13}$ | $1.80 \pm 0.35\,^{+0.53\,+0.30}_{-0.85\,-0.20}$ |
| (0.250–0.375) | $1.20 \pm 0.28\,^{+0.17\,+0.17}_{-0.36\,-0.14}$ | $1.64 \pm 0.33\,^{+0.52\,+0.24}_{-0.21\,-0.17}$ |
| (0.375–0.500) | $0.98 \pm 0.31\,^{+0.26\,+0.15}_{-0.26\,-0.11}$ | $1.58 \pm 0.38\,^{+0.33\,+0.21}_{-0.26\,-0.15}$ |
| (0.500–0.625) | $1.24 \pm 0.27\,^{+0.33\,+0.18}_{-0.24\,-0.12}$ | $1.92 \pm 0.34\,^{+0.52\,+0.28}_{-0.25\,-0.17}$ |
| (0.625–0.750) | $1.80 \pm 0.36\,^{+0.48\,+0.24}_{-0.20\,-0.19}$ | $2.97 \pm 0.44\,^{+0.30\,+0.37}_{-0.28\,-0.32}$ |
| (0.750–0.875) | $3.70 \pm 0.53\,^{+0.61\,+0.54}_{-0.65\,-0.37}$ | $6.34 \pm 0.65\,^{+0.62\,+0.61}_{-1.09\,-0.58}$ |
| (0.875–1.000) | $2.87 \pm 0.37\,^{+0.36\,+0.23}_{-0.33\,-0.18}$ | $3.86 \pm 0.42\,^{+0.45\,+0.27}_{-0.43\,-0.16}$ |
| (0.000–0.250) | $0.68 \pm 0.17\,^{+0.12\,+0.06}_{-0.19\,-0.09}$ | $1.10 \pm 0.20\,^{+0.35\,+0.26}_{-0.48\,-0.15}$ |
| (0.250–0.500) | $1.10 \pm 0.21\,^{+0.17\,+0.17}_{-0.23\,-0.14}$ | $1.63 \pm 0.25\,^{+0.26\,+0.24}_{-0.16\,-0.19}$ |
| (0.500–0.750) | $1.52 \pm 0.22\,^{+0.30\,+0.22}_{-0.17\,-0.16}$ | $2.43 \pm 0.27\,^{+0.30\,+0.34}_{-0.16\,-0.24}$ |
| (0.750–1.000) | $3.29 \pm 0.32\,^{+0.42\,+0.38}_{-0.31\,-0.35}$ | $5.10 \pm 0.38\,^{+0.41\,+0.44}_{-0.62\,-0.48}$ |

Table 4: The differential cross sections $d\sigma/dx_\gamma^{\rm OBS}$ for channel (1) as function of $x_\gamma^{\rm OBS}$ for the kinematic region $E_T^{jet1} > 7$ GeV, $E_T^{jet2} > 6$ GeV, as given in Fig.6, and for the kinematic region $E_T^{jet1} > 6$ GeV, $E_T^{jet2} > 5$ GeV. The $x_\gamma^{\rm OBS}$ range is given in brackets. The quoted cross sections correspond to the centres of the corresponding bins. The first error is statistical, the second is systematic and the third one is the energy scale uncertainty. Overall normalisation uncertainties due to luminosity measurement ($\pm 1.4\%$) and to $D^*$ and $D^0$ decay branching ratios ($\pm 3.7\%$) are not included in the systematic errors.

the total charm dijet cross section is $^{+6.4}_{-3.9}$%. For the $x_\gamma^{\rm OBS}$ differential cross sections they were added in quadrature to the statistical errors and are indicated as the outer error bars in Fig. 6. The energy scale uncertainty is shown as the shaded bands. Table 4 lists separately the statistical, systematic and energy scale uncertainties.

## 7.2 Comparison with Theoretical Predictions

In Fig. 6(a) the $d\sigma/dx_\gamma^{\rm OBS}$ distributions of the HERWIG MC simulation, normalised to the data, are shown for the LO-direct and LO-resolved contributions as well as for their sum. The fractions of each contribution was taken from the MC simulation. There is a peak in the data at high values of $x_\gamma^{\rm OBS}$, consistent with a large contribution from LO-direct photon processes. However, there is also a substantial tail to low $x_\gamma^{\rm OBS}$ values, which is not described by the LO-direct MC. Hence a LO-resolved component is required. In the LO-resolved MC histogram, the dominant contribution from photon charm excitation (lightly hatched) is distinguished from that of other LO-resolved photon processes (densely hatched). The contribution of $b$-quarks to $D^*$ production was taken into account in the MC sample as in the inclusive $D^*$ analysis. It is about 10% and approximately constant with $x_\gamma^{\rm OBS}$. The MC distributions, where the LO-resolved and LO-direct contributions are allowed to vary independently, were fitted to the data. The data require a LO-resolved contribution of $45 \pm 5$ $(stat.)$%. This value is consistent with the LO HERWIG prediction of 37%. The charm excitation contribution to the LO-resolved photon process in the HERWIG MC is 93%.

A comparison of the data with a NLO calculation for a charm dijet sample was performed using the massive charm approach [4]. This calculation does not have an explicit charm excitation component, since charm is not treated as an active flavour in the photon structure function. The $x_\gamma^{\rm OBS}$ distribution at the parton level was estimated by applying the KTCLUS jet finder to the two or three partons produced in this NLO calculation [30] for the kinematic region of our $D^*$ and associated dijet analysis. Here $\epsilon = 0.02$ was used and $m_\perp = \sqrt{m_c^2 + \langle p_\perp^2 \rangle}$, where $\langle p_\perp^2 \rangle$ is the average $p_\perp^2$ of the two charm quarks. The result of this calculation (full histogram) is compared to the data in Fig. 6b. To minimise migration effects due to hadronisation from high $x_\gamma^{\rm OBS}$, the data are given in wider bins compared to Fig. 6a. It can be seen that the NLO massive charm calculation [4] produces a tail towards low $x_\gamma^{\rm OBS}$ values similar to the light parton jet case [41]. However, there is a significant excess in the data over this NLO prediction. From MC studies we estimate that $\simeq 6\%$ of the highest $x_\gamma^{\rm OBS}$ bin ($0.75 < x_\gamma^{\rm OBS} < 1.0$) can migrate to the lower bins due to hadronisation effects. An effect of this size cannot explain the measured low $x_\gamma^{\rm OBS}$ cross section. Using $\mu_R = 0.5 m_\perp$ and $m_c = 1.2$ GeV in the calculation (dashed histogram) yields a higher $x_\gamma^{\rm OBS}$ tail, which is still below the data. With these parameters the cross section near $x_\gamma^{\rm OBS}$=1 is above the data. Applying an intrinsic transverse momentum $\langle k_T^2 \rangle = 1$ GeV$^2$ (section 6.1) increases the predicted cross sections in the two central $x_\gamma^{\rm OBS}$ bins. However the predicted cross sections are still below the measurement.

The conclusions drawn above are the same when: a) the hadron level jet cuts $E_T^{jet1}$ >6 GeV, $E_T^{jet2}$ >5 GeV (Table 4) were used; b) a cone jet algorithm [42] was applied instead of

a cluster algorithm; c) PYTHIA MC was used instead of HERWIG; d) the jet trigger described in section 2 was used instead of the nominal one.

The extent to which a NLO calculation of charm in association with dijets may describe the $d\sigma/dx_\gamma^{\rm OBS}$ distribution must await further theoretical developments. In particular additional contributions arising from a photon structure function require massless charm NLO predictions for $d\sigma/dx_\gamma^{\rm OBS}$.

# 8 Summary and Conclusions

The integrated and differential inclusive photoproduced $D^{*\pm}$ cross sections in $ep$ collisions at HERA have been measured with the ZEUS detector in the kinematic region $Q^2 < 1\,{\rm GeV}^2$, $130 < W < 280\,{\rm GeV}$, $p_\perp^{D^*} > 2\,{\rm GeV}$ and $-1.5 < \eta^{D^*} < 1.5$. The cross section $\sigma_{ep\to D^{*\pm}X}$=18.9 $\pm$ 1.2 $(stat.)^{+1.8}_{-0.8}$ $(syst.)$ nb was measured using the channel $D^{*+} \to D^0\,\pi_S^+ \to (K^-\,\pi^+)\,\pi_S^+$. A second $D^*$ decay channel has been studied, $D^{*+} \to D^0\,\pi_S^+ \to (K^-\,\pi^+\,\pi^+\,\pi^-)\,\pi_S^+$, and good agreement with the $K\pi$ channel has been found in the region of overlap ($p_\perp^{D^*} > 4\,{\rm GeV}$). The results are compared with massive and massless charm scheme QCD NLO predictions. The NLO calculations are generally below the measured cross sections, in particular in the forward direction. The results are sensitive to the parton density parametrisation of the photon used to calculate the cross section in the massless charm scheme.

A sample of inclusive dijet events with an associated $D^*$ meson has been used to measure the cross section $d\sigma/dx_\gamma^{\rm OBS}$ in the range $130 < W < 280\,{\rm GeV}$ and $Q^2 < 1\,{\rm GeV}^2$. The jets were reconstructed with the KTCLUS algorithm, requiring $|\eta^{jet}| < 2.4$ and at least one $D^*$ in the range $-1.5 < \eta^{D^*} < 1.5$ and $p_\perp^{D^*} > 3\,{\rm GeV}$. Cross sections are given for the kinematical regions $E_T^{jet1} > 7$ GeV, $E_T^{jet2} > 6$ GeV and $E_T^{jet1} > 6$ GeV, $E_T^{jet2} > 5$ GeV. A peak at high values of $x_\gamma^{\rm OBS}$ is seen, in agreement with the expectation for direct photon processes. A large cross section is also measured at low $x_\gamma^{\rm OBS}$, where resolved processes are expected to contribute significantly. A comparison of the $x_\gamma^{\rm OBS}$ distribution to MC simulations yields a contribution to the cross section of about 45% from LO-resolved photon processes and indicates the existence of charm excitation in the photon parton density. The data at $x_\gamma^{\rm OBS} < 0.75$ are higher than a NLO massive charm calculation at the parton level.

# 9 Acknowledgements

We would like to thank the DESY Directorate for their strong support and encouragement. The remarkable achievements of the HERA machine group were essential for the successful completion of this work and are greatly appreciated. We would like to thank M. Cacciari, S. Frixione and B. Kniehl for discussions and for providing their NLO calculations.

# References


[1] Ch. Berger and W. Wagner, Phys. Rep. 146 (1987) 1;
For a recent summary see S. Söldner-Rembold, hep-ex/9711005, Invited talk given at the XVIII International Symposium on Lepton Photon Interactions, Hamburg, Germany, July-August 1997.

[2] H1 Collaboration, T. Ahmed et al, Nucl. Phys. B 445 (1995) 195.

[3] ZEUS Collaboration, J. Breitweg et al, European Phys. Journal C1 (1998) 109.

[4] S.Frixione et al., Phys. Lett. B 348 (1995) 633;
S.Frixione et al., Nucl. Phys. B 454 (1995) 3.

[5] B.A.Kniehl et al., Z. Phys. C76 (1997) 689;
J.Binnewies et al., DESY 97-241, hep-ph/9712482, Phys. Rev. D (1998) in print;
B.A.Kniehl, private communication.

[6] J.Binnewies et al., Z. Phys. C76 (1997) 677.

[7] M.Cacciari et al., Phys. Rev. D55 (1997) 2736; ibid 7134;
M.Cacciari, private communication.

[8] See for example J.R.Forshaw, Photon'97 theory summary, Egmond aan Zee, The Netherlands, May 1997 (hep-ph/9707238).

[9] R.M. Barnett et al., Particle Data Group, Phys. Rev. D 54 (1996) 1.

[10] S. Nussinov, Phys. Rev. Lett. 35 (1975) 1672;
G.J. Feldman et al., Phys. Rev. Lett. 38 (1977) 1313.

[11] ZEUS Collaboration, J.Breitweg et al., Phys. Lett. B 401 (1997) 192.

[12] ZEUS Collaboration, M. Derrick et al., Phys. Lett. B 322 (1994) 287.

[13] ZEUS Collaboration, M. Derrick et al., Phys. Lett. B 293 (1992) 465.

[14] The ZEUS Detector Status Report 1993, DESY 1993.

[15] N. Harnew et al., Nucl. Instr. Meth. A 279 (1989) 290;
B. Foster et al., Nucl. Phys. B (Proc. Suppl.) 32 (1993) 181;
B. Foster et al., Nucl. Instr. Meth. A 338 (1994) 254.

[16] M. Derrick et al., Nucl. Instr. Meth. A 309 (1991) 77;
A. Andresen et al., ibid. A 309 (1991) 101;
A. Caldwell et al., ibid. A 321 (1992) 356;
A. Bernstein et al., ibid. A 336 (1993) 23.

[17] J. Andruszków et al., DESY 92-066 (1992);
ZEUS Collaboration, M. Derrick et al., Z. Phys.C 63 (1994) 391.

[18] F. Jacquet and A. Blondel, Proc. of the Study for an *ep* Facility for Europe, ed. U.Amaldi, DESY 79/48 (1979) 377.

[19] ZEUS Collaboration, M. Derrick et al., Phys. Lett. B 349 (1995) 225.

[20] S.Catani et al., Nucl. Phys. B 406 (1993) 187.

[21] S.D.Ellis and D.E.Soper, Phys. Rev. D 48 (1993) 3160.

[22] C. Peterson et al., Phys. Rev. D 27 (1983) 105.

[23] T. Sjöstrand, Comp. Phys. Comm. 82 (1994) 74.

[24] G. Marchesini et al., Comp. Phys. Comm. 67 (1992) 465.

[25] A.D. Martin, W.J. Stirling and R.G. Roberts, Phys. Lett. B 354 (1995) 155.

[26] M. Glück, E. Reya and A. Vogt, Phys. Rev. D 46 (1992) 1973.

[27] J.M. Butterworth, J.R. Forshaw and M.H. Seymour, Z. Phys. C 72 (1996) 637.

[28] ZEUS Collaboration, M. Derrick et al., Z. Phys. C 72 (1996) 399.

[29] H. Plothow-Besch, Int. J. Mod. Phys. A10 (1995) 2901.

[30] S. Frixione et al. Nucl. Phys. B 412 (1994) 225.

[31] OPAL Collaboration, K.Akerstaff et al., European Phys. Journal C1 (1998) 439.

[32] J. Chrin, Z. Phys. C 36 (1987) 163.

[33] L.V. Gribov, E.M. Levin and M.G. Ryskin, Phys. Rep. C 100 (1983) 1;
E.M. Levin, M.G. Ryskin Yu.M. Shabelskii and A.G. Shuvaev, Sov. J. Nucl. Phys. 53 (1991) 657.

[34] E.A. Kuraev, L.N. Lipatov and V.S. Fadin, Sov. Phys. JETP 45 (1977) 199;
Y.Y. Balitskii and L.N. Lipatov, Sov. J. Nucl. Phys. 28 (1978) 822.

[35] S.P. Baranov and N.P. Zotov, hep-ph/9806449 and Proceedings of the 6th International Workshop on Deep Inelastic Scattering and QCD, Brussels, April 1998, to be published.

[36] H.L. Lai et al., Phys. Rev. D 55 (1997) 1280.

[37] L.E. Gordon and J.K. Storrow, Z. Phys. C 56 (1992) 307.

[38] P. Aurenche et al., Z. Phys. C 64 (1994) 621.

[39] ZEUS Collaboration, M. Derrick et al, Phys. Lett. B348 (1995) 665.

[40] B.W. Harris and J.F. Owens, Phys. Rev. D 56 (1997) 4007.

[41] M. Klasen and G. Kramer, Phys. Lett. B366 (1996) 385.

[42] J.E.Huth et al., Proc. of the 1990 DPF Summer Study on High Energy Physics, Snowmass, Colorado, Ed. E.L.Berger, World Scientific, Singapore (1992) p.134.

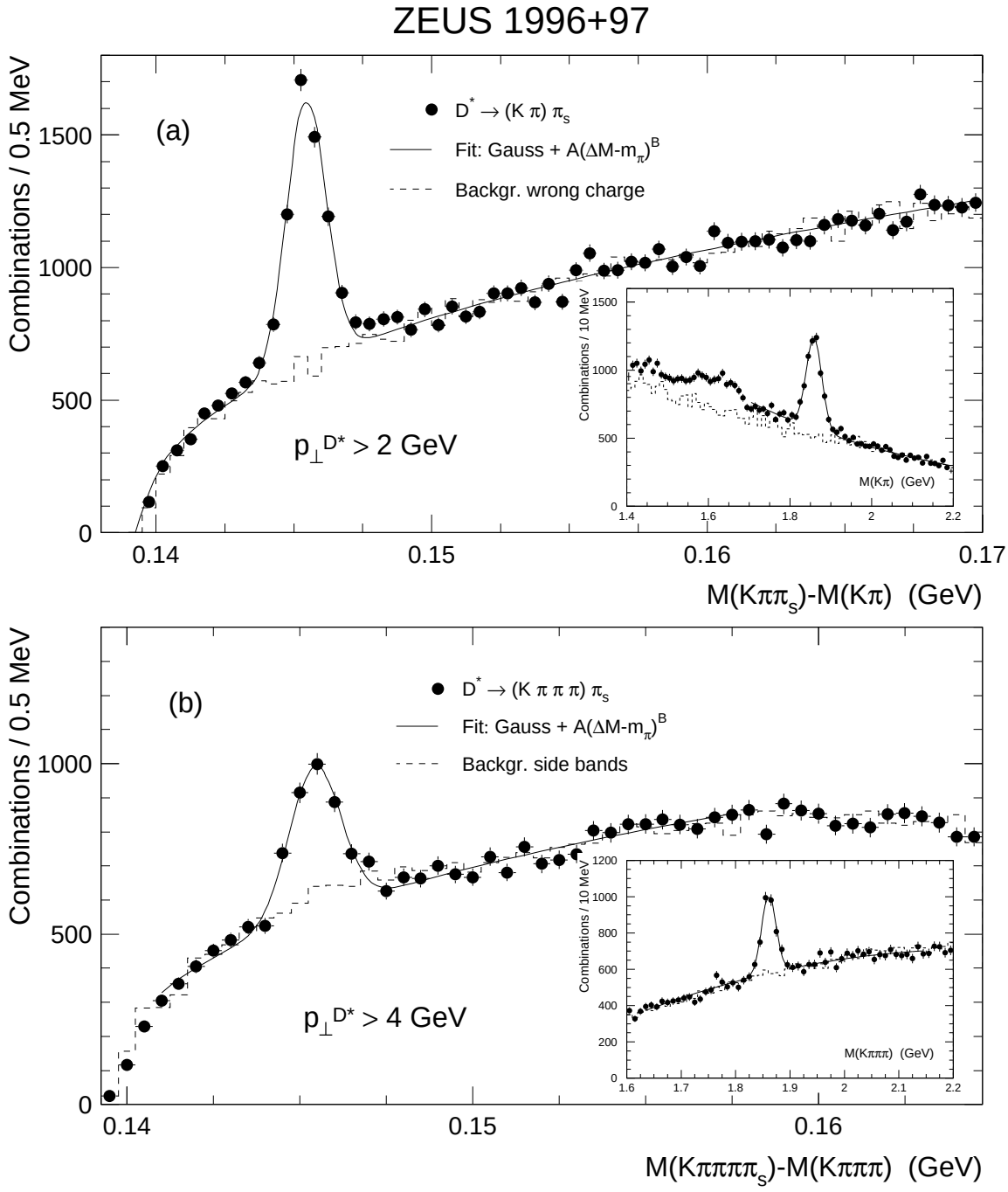


Figure 1: $\Delta M$ distributions (a) for the $(K\pi)\pi_S$ channel with $p_\perp^{D^*} > 2$ GeV and (b) for the $(K\pi\pi\pi)\pi_S$ channel with $p_\perp^{D^*} > 4$ GeV. The full dots are right charge combinations from the $D^0$ signal region ($1.80 - 1.92$ GeV). The dashed histograms are wrong charge combinations from the $D^0$ region for the $(K\pi)\pi_S$ channel and side bands combinations (see text) for the $(K\pi\pi\pi)\pi_S$ channel. The full lines are the results of fits to a sum of a Gaussian and the functional form $A \cdot (\Delta M - m_\pi)^B$. The insets in (a) and (b) are the $M(K\pi)$ and $M(K\pi\pi\pi)$ distributions from combinations having $143 < \Delta M < 148$ MeV. The dashed histograms are wrong charge and side bands combinations, respectively.

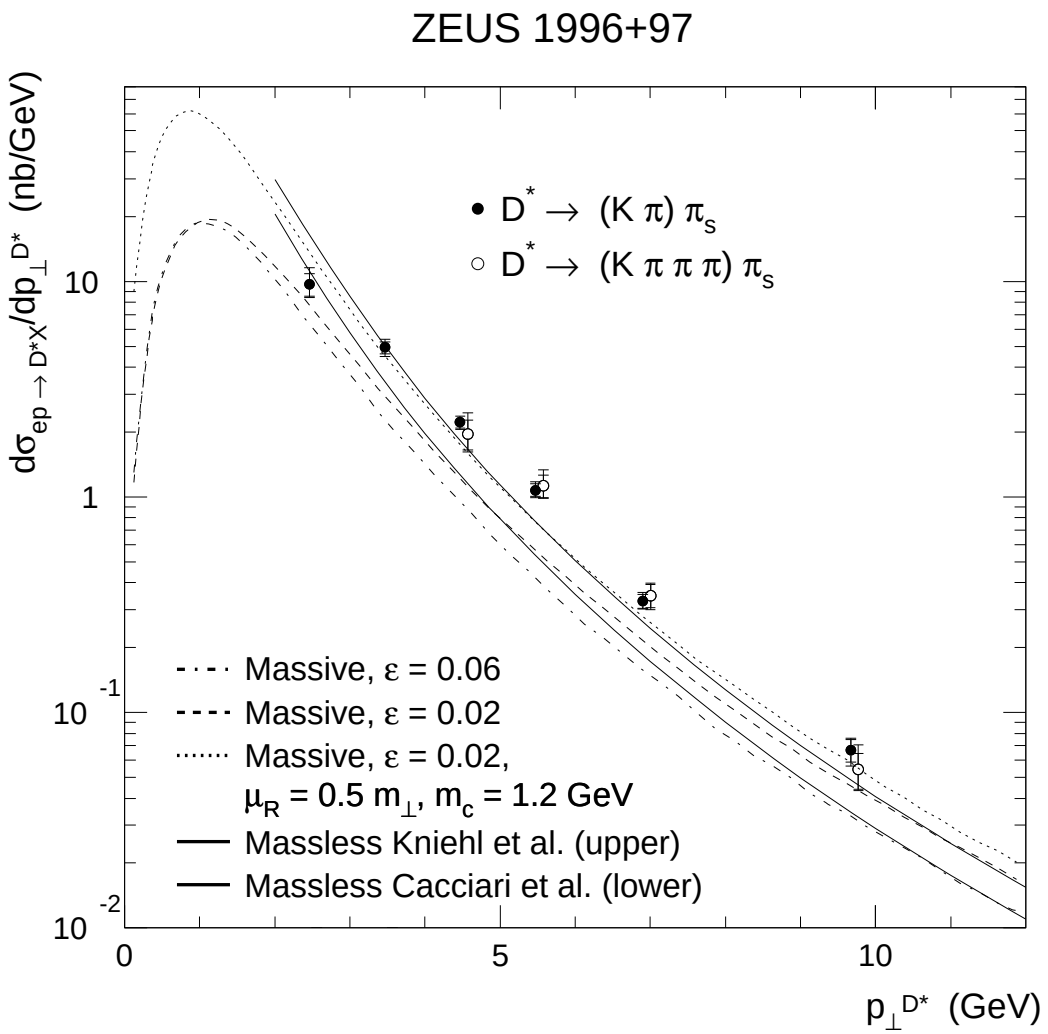


Figure 2: The differential cross section $d\sigma/dp_\perp^{D^*}$ for $D^*$ photoproduction, $Q^2 < 1\,\mathrm{GeV}^2$, in the kinematic region $130 < W < 280\,\mathrm{GeV}$ and $-1.5 < \eta^{D^*} < 1.5$ for the $(K\pi)\pi_S$ (full dots) and $(K\pi\pi\pi)\pi_S$ (open dots) channels. The $(K\pi)\pi_S$ points are drawn at the positions of the average values of an exponential fit in each bin. The $(K\pi\pi\pi)\pi_S$ points are offset for clarity. The inner part of the error bars shows the statistical error, while the outer one shows the statistical and systematic errors added in quadrature. The predictions of NLO perturbative QCD calculations are given by the dash-dotted, dashed and dotted curves for the massive charm approach [4] and by the full upper (lower) curve for the massless charm approach calculation of ref. [5] (ref. [7]), with the parameters described in section 6.

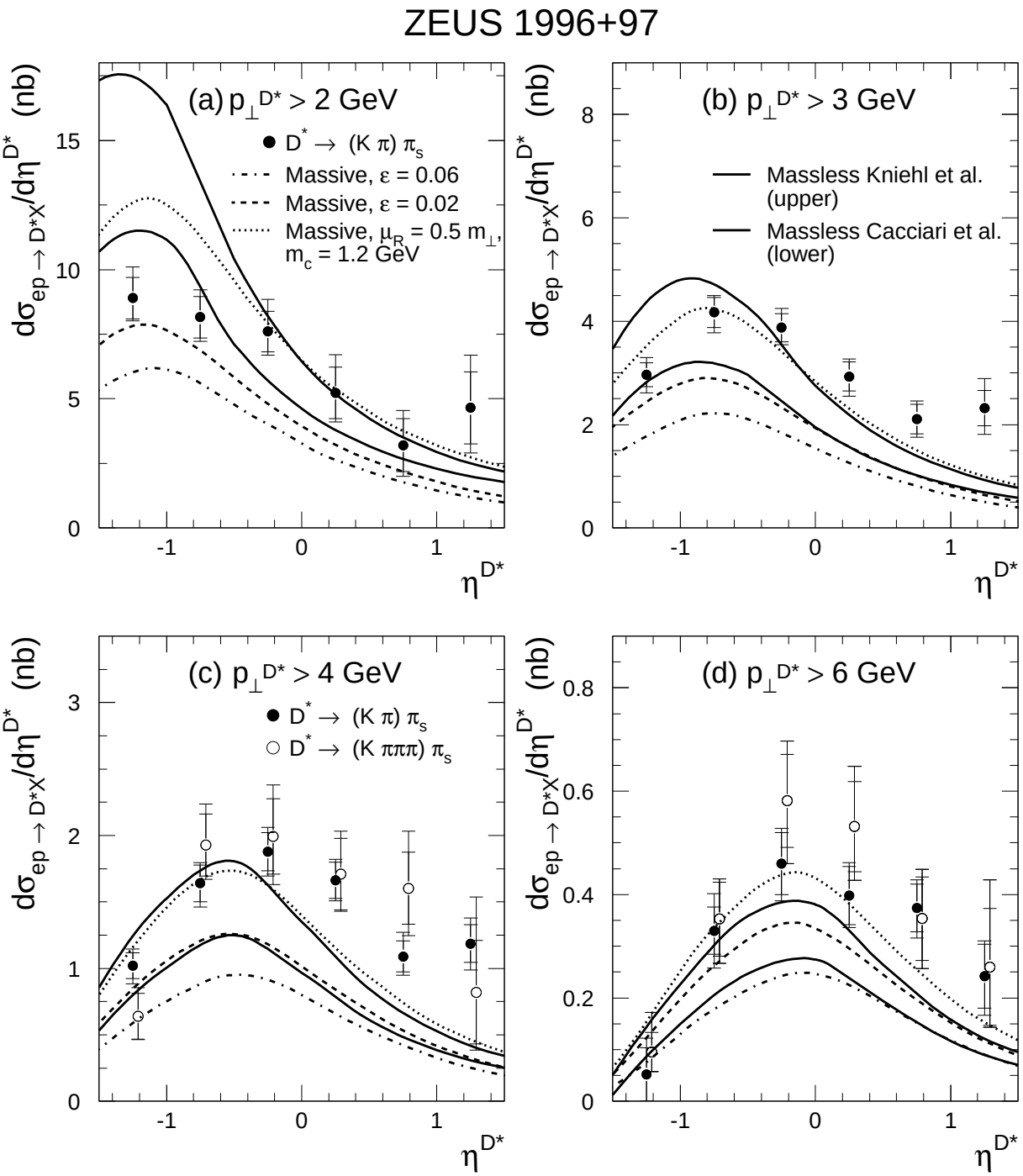


Figure 3: Differential cross sections $d\sigma/d\eta^{D^*}$ for $D^*$ photoproduction, $Q^2 < 1\,\mathrm{GeV}^2$ , in the kinematic region $130 < W < 280\,\mathrm{GeV}$ and a) $p_\perp^{D^*} > 2$ GeV; b) $p_\perp^{D^*} > 3$ GeV; c) $p_\perp^{D^*} > 4$ GeV; d) $p_\perp^{D^*} > 6$ GeV. The $(K\pi)\pi_S$ points are drawn at the centres of the corresponding bins. The $(K\pi\pi\pi)\pi_S$ points are offset for clarity. The inner part of the error bars shows the statistical error, while the outer one shows the statistical and systematic errors added in quadrature. The curves correspond to the same predictions of NLO perturbative QCD calculations as in Fig. 2.

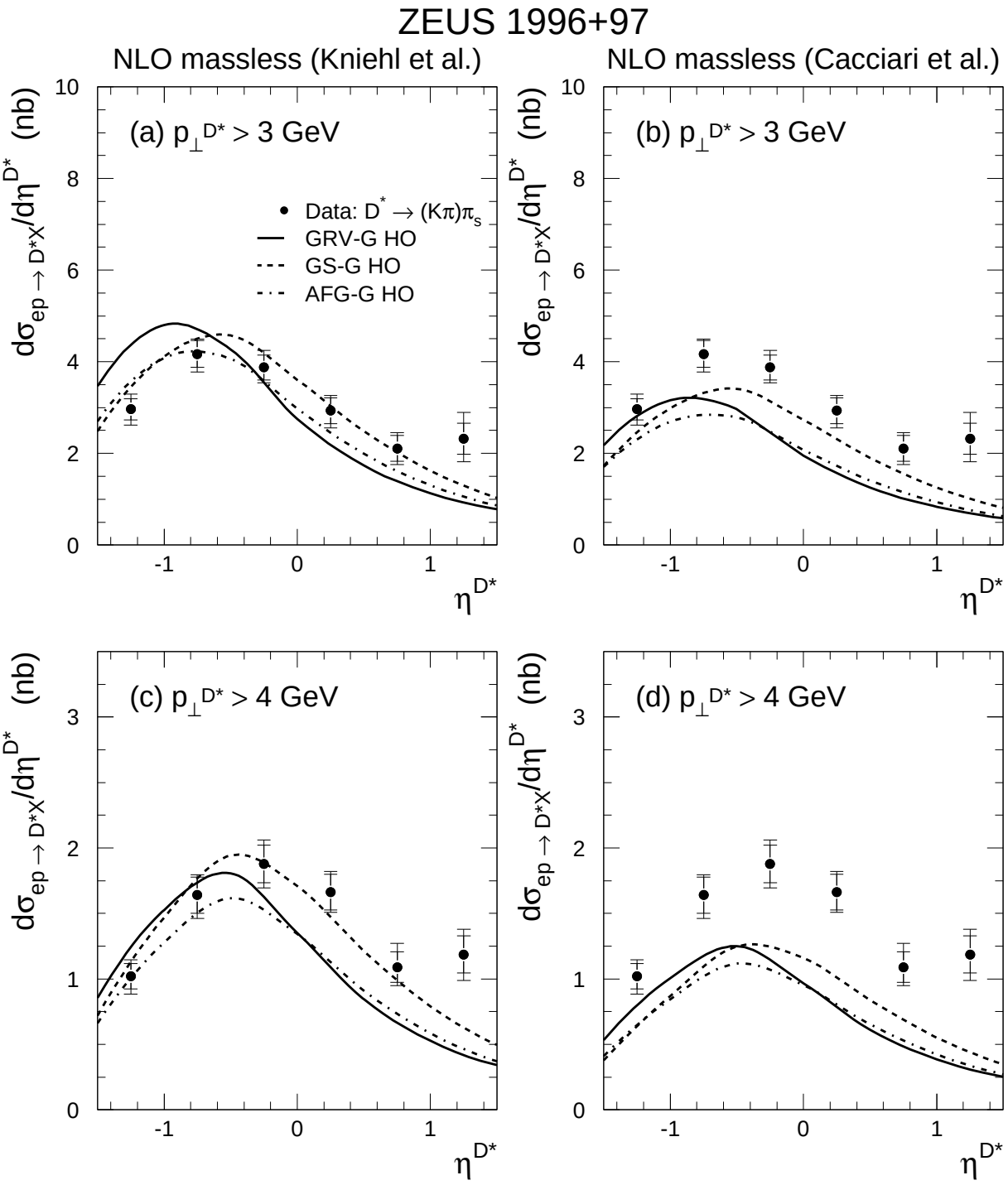


Figure 4: Differential cross sections $d\sigma/d\eta^{D^*}$ for $D^*$ photoproduction, $Q^2 < 1\,\mathrm{GeV}^2$ , in the kinematic region $130 < W < 280\,\mathrm{GeV}$ for the $(K\pi)\pi_S$ channel with (a-b)$p_\perp^{D^*} > 3$ GeV and (c-d)$p_\perp^{D^*} > 4$ GeV. The points are drawn at the centres of the corresponding bins. The inner part of the error bars shows the statistical error, while the outer one shows the statistical and systematic errors added in quadrature. The curves are the predictions of the massless charm NLO of ref. [5] (a,c) and ref. [7] (b,d) with various photon parton density parametrisations.

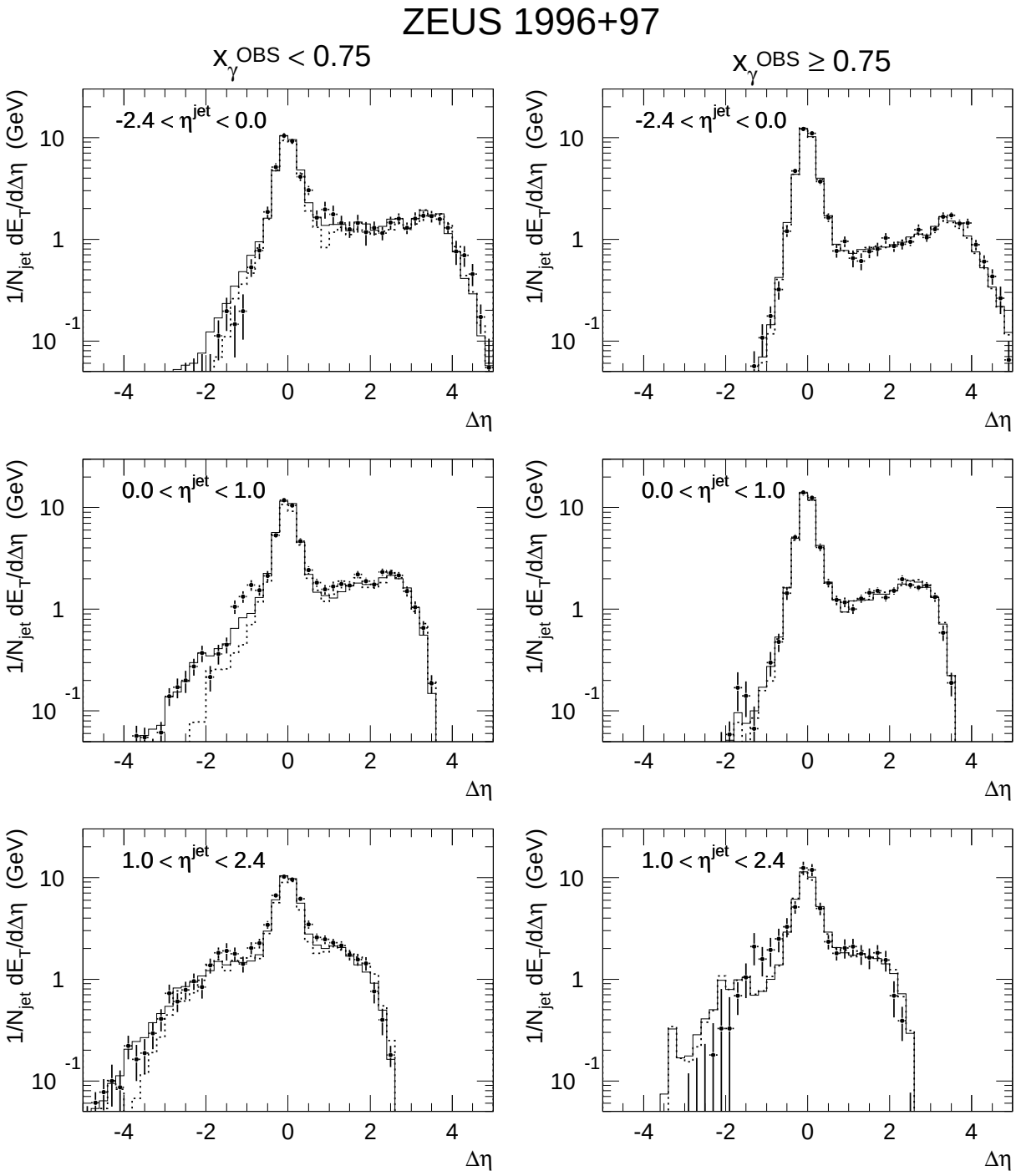


Figure 5: Uncorrected transverse energy flow with respect to the jet axis for dijet events containing a $D^*$ in a kinematic region given in the text and for $E_{T,cal}^{jet} > 4$ GeV. The jets are defined using the KTCLUS jet algorithm. The distributions are given in three regions of $\eta^{jet}$ separately for direct ($x_\gamma^{\rm OBS} \geq 0.75$) and resolved ($x_\gamma^{\rm OBS} < 0.75$) photon events. The data (dots) are compared to expectations of the HERWIG MC (full histogram) and LO-direct only (dotted histogram). The error bars represent the statistical uncertainty only.

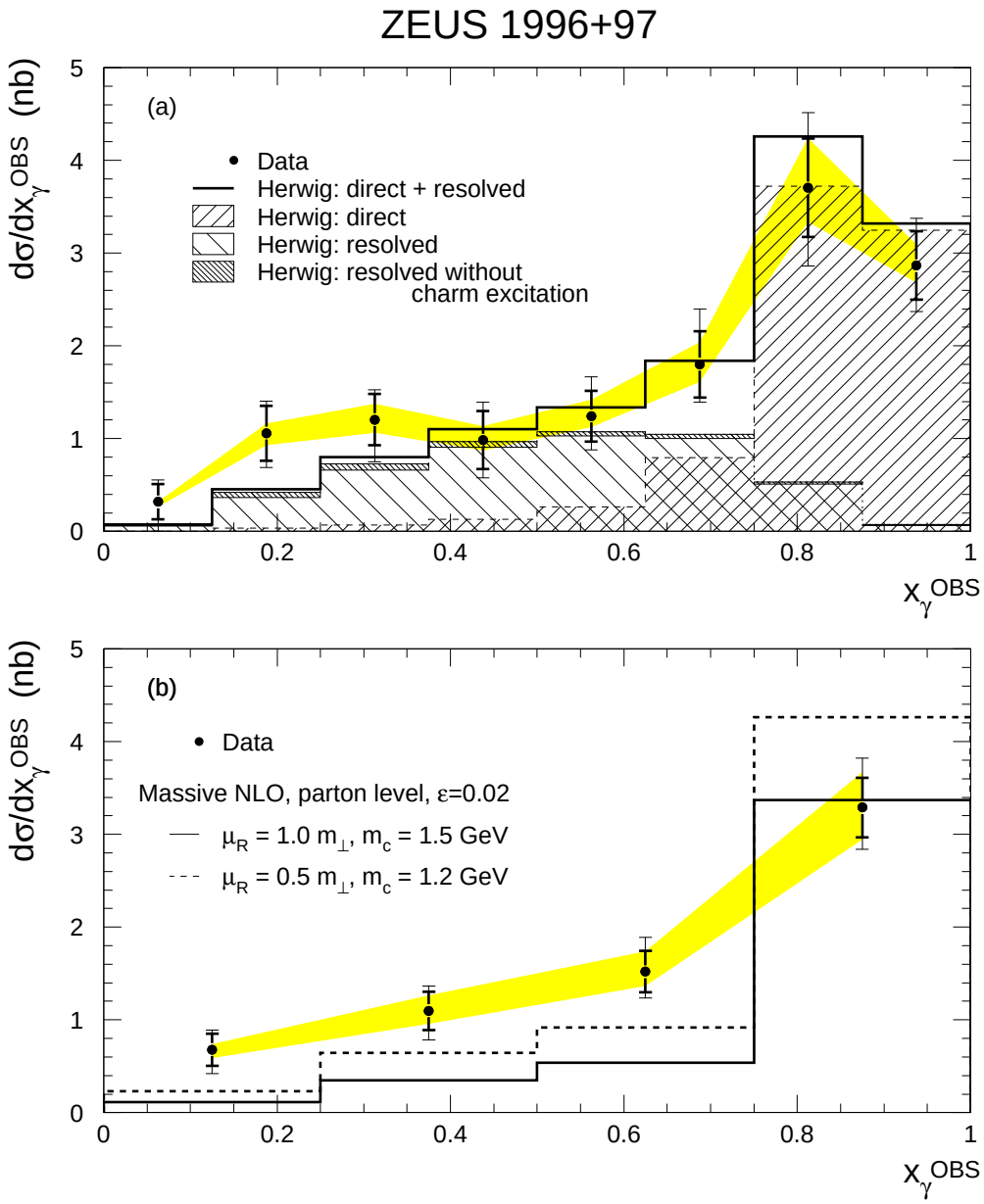


Figure 6: The differential cross section $d\sigma/dx_\gamma^{\rm OBS}$ for dijets with an associated $D^*$ meson with $p_\perp^{D^*} > 3$ GeV, $-1.5 < \eta^{D^*} < 1.5$ in the kinematic range $130 < W < 280$ GeV, $Q^2 < 1$ GeV$^2$, $|\eta^{jet}| < 2.4$, $E_T^{jet1} > 7$ GeV and $E_T^{jet2} > 6$ GeV. The KTCLUS algorithm is used for the jet definition. The points are drawn at the centres of the corresponding bins. The inner part of the error bars shows the statistical uncertainties. The outer part is the statistical and systematic errors added in quadrature. The energy scale uncertainty is given separately by the shaded bands. In (a) the experimental data (dots) are compared to the expectations of the HERWIG simulation, normalised to the data, for LO-direct (right hatched), LO-resolved (left hatched), LO-resolved without charm excitation (dense hatched) and the sum of LO-direct and LO-resolved photon contribution (full histogram). In (b) the data are compared with a parton level NLO massive charm calculation [4] with the parameters described in section 7.2.